



Published in final edited form as:

Cell Rep. 2023 June 27; 42(6): 112554. doi:10.1016/j.celrep.2023.112554.

Low-threshold, high-resolution, chronically stable intracortical microstimulation by ultraflexible electrodes

Roy Lycke^{1,2,8}, Robin Kim^{1,2,8}, Pavlo Zolotavin^{1,2}, Jon Montes^{2,3}, Yingchu Sun^{1,2}, Aron Koszeghy⁴, Esra Altun^{2,5}, Brian Noble^{2,6}, Rongkang Yin^{1,2}, Fei He^{1,2}, Nelson Totah^{4,7}, Chong Xie^{1,2,3,*}, Lan Luan^{1,2,3,9,*}

¹Department of Electrical and Computer Engineering, Rice University, Houston, TX 77005, USA

²Rice Neuroengineering Initiative, Rice University, Houston, TX 77005, USA

³Department of Bioengineering, Rice University, Houston, TX 77005, USA

⁴Helsinki Institute of Life Science (HiLIFE), University of Helsinki, 00790 Helsinki, Finland

⁵Material Science and NanoEngineering, Rice University, Houston, TX 77005, USA

⁶Applied Physics Program, Rice University, Houston, TX 77005, USA

⁷Faculty of Pharmacy, University of Helsinki, 00790 Helsinki, Finland

⁸These authors contributed equally

⁹Lead contact

SUMMARY

Intracortical microstimulation (ICMS) enables applications ranging from neuroprosthetics to causal circuit manipulations. However, the resolution, efficacy, and chronic stability of neuromodulation are often compromised by adverse tissue responses to the indwelling electrodes. Here we engineer ultraflexible stim-nanoelectronic threads (StimNETs) and demonstrate low activation threshold, high resolution, and chronically stable ICMS in awake, behaving mouse models. *In vivo* two-photon imaging reveals that StimNETs remain seamlessly integrated with the nervous tissue throughout chronic stimulation periods and elicit stable, focal neuronal activation at low currents of 2 μ A. Importantly, StimNETs evoke longitudinally stable behavioral responses for over 8 months at a markedly low charge injection of 0.25 nC/phase. Quantified histological

This is an open access article under the CC BY-NC-ND license (<http://creativecommons.org/licenses/by-nc-nd/4.0/>).

*Correspondence: chongxie@rice.edu (C.X.), lan.luan@rice.edu (L.L.).

AUTHOR CONTRIBUTIONS

Conceptualization, L.L. and C.X.; methodology, L.L., C.X., R.L., R.K., P.Z., J.M., A.K., N.T., and Y.S.; investigation, R.L., R.K., and J.M.; writing – original draft, R.L., R.K., and L.L.; writing – review & editing, L.L., C.X., R.L., R.K., N.T., P.Z., A.K., F.H., and R.Y.; funding acquisition, C.X. and L.L.; resources, R.L., R.K., P.Z., J.M., Y.S., A.K., E.A., B.N., R.Y., and F.H.; visualization, R.L. and R.K.; supervision, L.L., C.X., and N.T.; project administration, L.L. and C.X. The two co-first authors R.L. and R.K. have contributed equally to this work and are allowed to list themselves as first authors in their CVs.

DECLARATION OF INTERESTS

C.X. and L.L. and are co-inventors on a patent filed by The University of Texas (WO2019051163A1, March 14, 2019) on the ultraflexible neural electrode technology described in this study. L.L., C.X., and P.Z. hold equity ownership in Neuralthread, Inc., an entity that is licensing this technology.

SUPPLEMENTAL INFORMATION

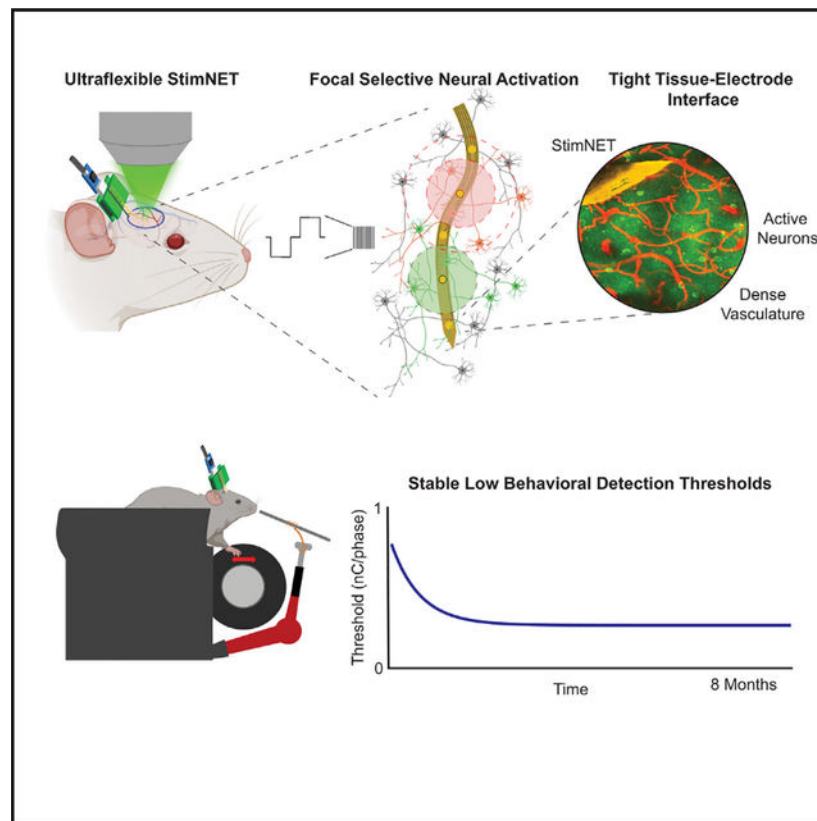
Supplemental information can be found online at <https://doi.org/10.1016/j.celrep.2023.112554>.

analyses show that chronic ICMS by StimNETs induces no neuronal degeneration or glial scarring. These results suggest that tissue-integrated electrodes provide a path for robust, long-lasting, spatially selective neuromodulation at low currents, which lessens risk of tissue damage or exacerbation of off-target side effects.

In brief

Lycke et al. have developed ultraflexible microstimulation electrodes that elicit focal neuronal activation and behavioral detection at low currents, integrate seamlessly with nervous tissue, and are chronically robust and stable. The study provides a path to safe, long-lasting, and precise neuromodulation for neuroprosthetics and circuit manipulations.

Graphical Abstract



INTRODUCTION

Built upon the success of electrical stimulation from macroelectrodes to induce coarsely focused cortical activation,^{1,2} intracortical microstimulation (ICMS) using implanted microelectrodes modulates neural activity and elicits behavioral responses at finer spatial resolutions.^{3–8} In ICMS, intracortically implanted microcontacts inject electrical charges into the surrounding tissue, create flow of ionic current, depolarize the membranes of excitable cells, and change neural activity locally. This capability enables diverse applications such as establishing causal links between neural activity and behavior,^{3,9,10}

modulating attention and learning,¹¹ and producing perception and sensations.^{12–17} Across all these diverse applications, the overall technological goal of ICMS is to produce targeted, high-resolution neuronal modulation capable of eliciting stable perception or sensation over an extended period.^{18,19} Because ICMS often induces neuronal activation from the passage of axons,²⁰ realizing this goal requires (1) subcellular proximity and stability at the tissue-electrode interface and (2) the stimulation electrode to reliably produce identical, highly localized charge injections.

Current ICMS electrodes are significantly more rigid than the host brain tissue, resulting in instability of the tissue-electrode interface and substantial “spatiotemporal blur” in the neuronal response.²¹ Over chronic implantation durations, the tissue-electrode interface deteriorates.^{22–24} Neuronal degeneration and formation of glial scarring around the probe²⁵ alter the electric fields induced by the stimulus, which could change the resultant neural²⁶ and behavioral^{27–30} responses. Likely related to interface degradation, large and increasing stimulation amplitudes^{26,27} are often needed to maintain behavioral responses in chronic applications, which expedites the deterioration of stimulating electrodes³¹ and increases the risk of tissue damage.^{32,33} In a recent case where the detection thresholds did not increase with time, large day-to-day variations were observed.¹⁷ It is not clear whether the notable variations were due to changes in adverse tissue responses, degradation of electrodes, or intrinsic changes in the excitability or functional response of the neural tissue.

Intuitively, promoting device-tissue integration could provide one approach to improve the resolution and stability of ICMS by enhancing electrode-neuron proximity.¹⁸ Based on fundamental biophysical principles, implants with no glial scar encapsulation will minimize the separation between the electrode and the targeted neurons, which will reduce the activation threshold, decrease the number of activated neurons at threshold, improve focality, eliminate time-varying foreign-body tissue responses, and result in high-resolution, chronically stable neuromodulation (Figure 1A). Experimentally, improving device-tissue integration has markedly improved recording efficacy, density, and longevity.^{34,35} However, the impact of an intact tissue-device interface on ICMS has not been established. In this work, we engineered device flexibility and developed the ultraflexible stimnanoelectronic thread (StimNET) to meet the requirements of robust charge injection and subcellular stability at the tissue-electrode interface simultaneously. We employed a suite of optical, electrical, behavioral, and histological methods in mouse models to evaluate the efficacy, resolution, stability, and tissue compatibility of neuromodulation. We verified that these tissue-integrated electrodes produce spatially confined neuronal activation and elicit longitudinally stable behavioral detection at substantially reduced stimulation currents with no neuronal degradation or glial scarring. These results highlight the importance of tight tissue-electrode integration in the efficacy of stimulation and provide a path for long-lasting, high-resolution neuromodulation at low currents that minimize the risk of tissue deterioration or exacerbation of off-target side effects.

RESULTS

Engineering ultraflexible StimNETs for robust charge injection

We first performed proof-of-principle finite-element-model simulations to compare the activation threshold of neurons at various glial scar thicknesses (0, 20, and 40 μm). The absence of glial scarring reduces the current required to activate the same number of neurons and lowers the tissue volume of activation (Figure 1B). This effect scales with the thickness of the glial scar: the thinner the scar, the smaller the current required to stimulate neurons in the non-scarred tissue and the smaller the gross volume of total tissue activation (both neuronal and glial scar tissue) at the threshold. Equivalently, when activating the same tissue volume not occupied by glial scarring, the spread of current is smaller without glial scarring. Furthermore, because the spread of current is reduced by reducing the glial scar, the spatial overlap of tissue activation when stimulating two nearby contacts is reduced (Figure 1C). Closely spaced stimulation sites with no scar encapsulation provide the most spatially distinct tissue activation compared with those with scars at the same tissue activation volume.

The results from numerical simulations motivated us to maximize the efficacy of ICMS by optimizing the tissue-electrode interface. We chose to drastically reduce the substrate thickness of intracortical electrodes to minimize the bending stiffness and provide tight tissue-electrode integration. Our previous study demonstrated that nanoelectronic threads (NETs) at a total thickness of 1 μm form an intimate tissue-electrode interface during chronic implantation, featuring an intact brain-blood barrier, tissue-electrode stability at the subcellular scale, and an absence of neuronal degradation and glial scarring near the electrodes.^{36,37} However, the ultrathin insulation layer (0.5 μm) and multilayer device architecture impose significant challenges for lasting stimulation without structural and functional breakdown. Through iterative testing and device optimization we have realized ultraflexible StimNETs for robust stimulation at similar form factors and with similar ultraflexibility compared with the recording NETs (Figure 1D). We focused on the following modifications. First, to reduce the risk of cross talk between nearby trace lines and improve biocompatibility, we switched the substrate material from SU-8 photoresist to polyimide (PI), which is a stronger dielectric with larger tensile strength, and adapted multilayer planar microfabrication on PI (STAR Methods). Second, to improve the charge storage capacity and charge injection capacity of NET microcontacts, we sputtered IrO_x on Au contacts at the wafer scale during microfabrication.³⁸ Third, as a precaution to cover potential cracks on IrO_x vertical walls, we offset vias and contacts. Last, and importantly, to alleviate the risk of delamination, we microfabricated a cap ring (thickness of 0.3 μm) using PI surrounding each contact on top of the IrO_x as an additional mechanical reinforcement (Figure 1D). The optimized StimNET has a shank thickness of 1 μm and an additional 0.3 μm thickness at the cap ring, a width of 100 μm tapering to 36 μm over the 1,800 μm functional length of the implant. Each device has 32 individually addressed microcontacts for both recording and stimulation at a diameter of 24 μm . The center-to-center spacing between adjacent contacts is 60 μm .

To verify the charge injection and storage capacity of StimNETs, we performed voltage transient measurements and cyclic voltammetry (CV) *in vitro* (STAR Methods). Individual microcontacts in StimNETs output currents up to 50 μA while maintaining the maximum cathodically and anodally driven electrochemical potential excursion within the water window of $[-0.6 \text{ to } 0.8 \text{ V}]$ (Figure 1E), e.g., the maximum polarizations across the electrode-electrolyte interface were the most negative polarization E_{mc} at $-0.41 \text{ to } -0.04 \text{ V}$ and the most positive polarization E_{ma} at $0.22 \text{ to } 0.4 \text{ V}$ for all currents. The charge injection capacity of StimNETs is 1.1 mC/cm^2 , which is on par with the typical charge injection capacity of rigid electrodes with sputtered IrO_x , cathodal first pulsing, and no voltage biasing (e.g., 0.9 mC/cm^2 as in Cogan et al.³⁹). Figure 1F shows a representative pulsing test in which we stimulated a contact site at 500 Hz, with 30 μA biphasic charge-balanced pulses for 50 million pulses, and acquired CV at a scan rate of 100 mV/s periodically during pulsing. Except for an initial increase in charge storage capacity, which is well documented as increased porosity and accessibility of $\text{Ir}^{3+}/\text{Ir}^{4+}$ redox sites with continual oxidation,⁴⁰ there was little change in CV between 2.5 million and 50 million stimulation pulses. These results demonstrated the high charge injection and storage capacity of StimNETs and supported their durability and robustness during stimulation.

High-throughput quantification of ICMS-evoked neuronal activation in awake animals

To evaluate ICMS efficacy over a chronic period at the single-cell resolution, we co-implanted a cranial window and StimNET in the somatosensory cortex of Thy1-GCamp6s mice and performed two-photon (2P) Ca^{2+} imaging during ICMS (Figure 2A, STAR Methods) at least 2 weeks following implantation, at which time the surgical trauma had subsided.⁴¹ Different from most prior studies of the spatial activation pattern of ICMS, which used anesthetized animals,^{20,42} we performed 2P z-stack imaging of neuronal activations in awake animals to remove the confounding effects of anesthesia. We continuously stimulated at 50 Hz while simultaneously acquiring z stacks of $1 \times 1 \times 0.4 \text{ mm}$ (at the z spacing of 2 μm) that took about 30 s each (STAR Methods). The stimulation paradigm is insensitive to the temporal response to a singular pulse but allows for accurate quantification of the volumetric population of neurons consistently active during the stimulation: 50 Hz stimulation induces a relatively fast rise time of Ca^{2+} fluorescence,⁴² and continuous stimulation for 30 s allows time to complete the z stack at a 30 Hz frame rate and with four-frame averaging to enhance signal-to-noise ratio. We focused on quantification of the populational activation and did not analyze temporal dynamics in this study.

Figure 2B shows a set of representative Ca^{2+} images across the cortical depth acquired during stimulation where cells were fluorescent due to either spontaneous or ICMS-evoked activation. To quantify the ICMS-evoked neuronal activation from the background of spontaneous activity, we used a trial structure where the randomized ICMS trials alternated with baseline trials (spontaneous activity, no stimulation) for differential measurements and analysis between each pair of stimulated and baseline trials (STAR Methods). Using customized automatic data acquisition pipelines, we were able to acquire 300–400 z stacks in a typical 3 h session that contained blocks of randomized stimulation channels and currents and seven to nine replicas of these blocks. Representative trials of four current

levels and three stimulation channels showed clear modulation of Ca^{2+} fluorescence (Figure 2C; trial sequences were recognized and grouped by current and stimulation channel for presentation clarity).

We then developed and used computationally efficient matrix manipulations to calculate the difference between paired stimulation and baseline, identified the voxels that were activated by any current and stimulation site, quantified the probability of activation across n repeats, and imposed a probability threshold (here we set as 75%) across all trials to identify areas that were consistently activated only upon stimulation (Figure 2D). The most computationally demanding step, segmentation to identify individual neurons evoked by ICMS, was performed only once, aggregating all trials in the same imaging section together. This pipeline greatly improves the throughput of imaging processing, making it feasible to identify individual neurons and their location in three dimensions (3D) under numerous stimulation parameters (STAR Methods). In addition, because the activation regions are identified all together for all trials that use different stimulation sites and at various ICMS currents before segmentation, the segmented neurons are less prone to small drifts, which facilitates the comparison of neuronal activation pattern across stimulation sites and currents (STAR Methods).

StimNET elicits spatially localized neuronal activation at low currents

To map the 3D spatial distribution of neuronal activation, we stimulated individual sites of StimNET in layer 2/3 in the somatosensory cortex, performed concurrent 2P z-stack imaging during ICMS up to 500 μm deep into the tissue, and identified the evoked neurons and their locations. We detected activation of a small number of cells near the electrodes at a low ICMS current of 2 μA (Figure 3A). Intuitively, the number of ICMS-evoked neurons increased with ICMS currents (Figure 3B; Kruskal-Wallis test with Dunn's *post hoc* correction, degrees of freedom (df) = 3, 2 μA vs. 5 μA , $p = 3.7\text{e-}9$; 2 μA vs. 7 μA , $p = 3.7\text{e-}9$; 2 μA vs. 10 μA , $p = 3.7\text{e-}9$). We compared the numbers and locations of neurons activated by the same stimulation site at four current levels (2, 5, 7, and 10 μA) to determine the ratio of neurons consistently activated at two adjacent current levels, e.g., the fraction of neurons activated at 2 μA that was also activated at 5 μA . At all three current pairs we tested, at least 85% of neurons activated by lower currents were also activated by the higher current (Figure 3B), supporting short-term stability of the tissue-electrode interface due to the mechanical compliance of StimNETs. Furthermore, we quantified the volumetric neural activation density (Figure S1) as a function of currents and projected the 3D activation density into 2D for visualization (Figure 3C; averaging 5 animals, 11 imaging sessions, and 21 stimulation sites). The neuronal activation was highly localized near the stimulation site at 2 μA , a low current that was rarely studied previously. Once the current increased to 5 μA and above, the currents required to induce neuronal activation in previous studies, the activation pattern became spatially distributed just as demonstrated in previous studies,^{20,43} with a high density of activation proximal to the stimulating electrode and sparse activation beyond 200 μm . Consistently, the spatial extent of ICMS-evoked neural activation, defined as the largest distance from any evoked neuron to the stimulation site, increased significantly from 2 to 5 μA (Figure 3D; Kruskal-Wallis test with Dunn's *post hoc* correction, df = 3, $p = 0.035$), but remained relatively unchanged with further increase in ICMS current (7 μA vs.

10 μA , $p = 0.90$). As a direction comparison, Neuronexus probes (rigid silicon electrodes) required a much higher current of 15–30 μA to elicit distinguishable neuronal activation in awake animals.⁴⁴ These experimental results supported our simulation (Figure 1B) and confirmed that the ultraflexible StimNET could elicit focal activation at very low currents.

Neuronal activation is spatially selective and numbers of evoked neurons are longitudinally stable

Most applications of ICMS will gain from the ability to activate discrete groups of neurons by neighboring contacts over an extended period. Therefore, we evaluated the spatial selectivity of StimNET, the ratio of the distinctive population activated by each contact over the total activation population, through longitudinal 2P Ca^{2+} imaging (STAR Methods). Spatial selectivity would be 1 if two nearby contacts resulted in entirely different, non-overlapping activation of neurons, while selectivity would be 0 if they activated the exact same population. Figure 3E shows are presentative neuronal activation pattern when stimulating two spatially adjacent contacts at 5 μA . The center-to-center distance was estimated to be 60 μm as defined by microfabrication, because our implantation protocol induces minimal deviation, which was demonstrated in our previous work.^{41,45} Each contact elicited distinctive neuronal activation, and only a small number of cells were co-activated by both contacts. To quantify how spatial selectivity changes with ICMS current and separation of stimulating contacts, we stimulated and simultaneously imaged volumetrically at four levels of currents and three contact distances. At a low stimulation current of 2 μA , the spatial selectivity was >95%, even for contacts that were separated by merely 60 μm center to center (36 μm edge to edge). As expected, increasing stimulating currents significantly decreases selectivity for all the contact spacing tested (Figure 3F; Kruskal-Wallis test, $\chi^2 = 136.24$, $p = 2.4\text{e-}29$, $df = 3$). Particularly, the lowest current has the highest spatial selectivity (Kruskal-Wallis test with Dunn's *post hoc* correction, 2 μA vs. 5 μA , $p = 0.0002$; 2 μA vs. 7 μA , $p = 3.7\text{e-}9$; 2 μA vs. 10 μA , $p = 3.7\text{e-}9$). For any given stimulation current, increasing the contact separation improves selectivity (Kruskal-Wallis tests with Dunn's *post hoc* correction, $df = 2$; 60 μm vs. 240 μm at 2 μA , $p = 0.02$, and at 10 μA , $p = 9.8\text{e-}12$). Notably, a 120 μm center-to-center separation was sufficient to achieve >90% spatial selectivity for all currents tested, which validates the application of StimNET for highly selective neuromodulation.

We repeated Ca^{2+} imaging longitudinally during stimulation until the cranial window got cloudy, which in this cohort of animals occurred approximately 9 weeks post-implantation. From the longitudinal imaging series, we mapped the neuronal activation spatially and quantified the number of neurons being activated and the spatial selectivity when stimulating two neighboring contacts as a function of time after StimNET implantation. The spatial patterns of neural activation evoked by the same stimulation sites and currents were similar across time, while the actual neurons activated from week to week by each contact had mild changes (Figure 3H). The number of neurons activated at the same current and the spatial selectivity at the same stimulation parameters remained stable throughout the entire experimental duration (Figure 3G). These results suggest that over chronic periods the same currents from StimNET activated similar numbers of neurons and maintained the same high level of spatial selectivity.

StimNET elicits robust, chronically stable behavioral detection at low currents

To evaluate the behavioral detectability of low-amplitude ICMS via chronically implanted StimNETs, we developed and used a go/no-go task, for which water-deprived, head-fixed mice were trained to turn a wheel past an angular displacement threshold in response to ICMS to obtain water rewards (STAR Methods; Figure 4A). The behavioral testing started several weeks after StimNET implantation and lasted for up to 226 days ($n = 5$). The last day of behavioral testing corresponds to day 308, 294, 284, 264, and 242 post-implantation for mice 1–5. We used a stimulation frequency of 100 Hz, a frequency commonly used in ICMS experiments performed in human patients.^{15–17} A random intertrial interval (2–6 s) prevented the mice from turning based on temporal expectation of ICMS (Figure 4B). We ensured that turning was not random, but was an ICMS stimulus-guided response by training the mice to suppress impulsive turns in the pre-stimulation period (Figure 4B, inset). A representative psychometric curve (Figure 4C) shows that motivation was high throughout the task (100% responses to suprathreshold stimuli occurring at random trials), and impulsive and random turning was rare (close to 0% at subthreshold stimuli). To efficiently and accurately measure behavioral detectability across multiple sites, we used an adaptive staircase method,⁴⁶ in which the amplitude of ICMS was raised or lowered based on the animal's performance to estimate the threshold^{46,47} (STAR Methods). In a representative example shown in Figure 4D, the stimulation currents in the last four reversals were 1 μA (all no responses) and 2 μA all responses), resulting in a detection threshold of 1.5 μA . This high-throughput method allowed us to quantify the threshold of 10–17 contacts spanning the cortical depth individually in one session.

We first concatenated all measurements from the entire experimental duration of up to 226 days and examined the behavioral detectability as a function of cortical depth. We identified significant differences in thresholds across cortical layers (Figure 4E; Kruskal-Wallis test, $\chi^2 = 707.84$, $p < 0.001$, $df = 4$). Paired comparisons using Dunn's *post hoc* correction showed that shallow cortical layers L1 and L2/3 had significantly higher detection thresholds than deeper cortical layers L4–L6 (L1 vs. L4, $p < 0.001$; L1 vs. L5, $p < 0.001$; L1 vs. L6, $p < 0.001$; L2/3 vs. L4, $p < 0.001$; L2/3 vs. L5, $p < 0.001$; L2/3 vs. L6, $p < 0.001$), and L4 had the lowest threshold. The layer difference in detection thresholds was similar to other ICMS behavioral studies using rigid laminar probes.⁵³ Critically, the behavioral detection threshold by StimNET was low. Figure 4F shows the thresholds identified using all contacts in L4–L6 from all measurement sessions (38 contacts, 362 sessions in total). The mean thresholds of all five animals were 1.12, 0.35, 0.88, 1.14, and 0.37 nC/phase, respectively, three of which were lower than 1 nC/phase. The lowest single measurement thresholds of each animal were 0.21, 0.08, 0.17, 0.33, and 0.17 nC/phase, all of which were much smaller than 0.5 nC/phase. Particularly, the lowest measured value across subjects and sessions was 0.08 nC/phase (0.5 μA) in mouse 2, the precision of which was limited by the current resolution of our stimulator at 1 μA . The last four reversals of the staircase method had currents at either 0 (100% no response) or 1 μA (100% response), resulting in a current threshold of 0.5 μA (Figure S2).

We then scrutinized the time dependence of behavioral detectability of ICMS using StimNET contacts in the deeper cortical layers L4–L6. Because contacts in L4, L5, and L6

provided relatively low detection thresholds, we analyzed all the data from L4–L6 together without distinguishing the fine depth difference. In all animals, the detection threshold, averaged among all stimulation sites in L4–L6, had an initial decay that can be described empirically as an exponential curve in the first 20–70 days. The threshold remained stable with little variation for a long period (Figure 4G). The stable phase had a much lower charge injection threshold than the initial phase, during which the detection threshold decreased. The longitudinal stability of detection threshold from a selection of individual channels was also superior. In the two examples in Figure S3A, the threshold remained unchanged for most of the days and changed by at most 1 μA for periods of 153 days (mouse 5) and 226 days (mouse 2). To ensure the reliability of this result, we examined the stimulation currents in the last four reversals of the staircase method that led to the quantification of the threshold (Figure S3B). About 80% of the last four reversals varied by only 1 μA (the resolution of our stimulator) between go responses and no-go responses, supporting the high-fidelity detection throughout all sessions.

Notably, in two animals (mice 2 and 5), a very low current of 1.5 μA (0.25 nC/phase) from a single stimulation site was sufficient to elicit and maintain robust behavioral detection over the long period (Figure S3A). This provides the lowest threshold of chronic ICMS studies in either behavior detection or neuronal activation to the best of our knowledge (Figure 4H). Furthermore, we explored if we could further reduce the overall charge injection by changing the stimulation frequency. We mapped the frequency-threshold dependence (Figure S4) and found that by using a low frequency of 6 Hz, we reduced the charge injection per second by an order of magnitude at mildly elevated current threshold (Figure 4H). Our stimulation parameters were well below the damage threshold of charge density, defined by Shannon's criteria at typical k constant values of $k = 1, 1.5, \text{ and } 2$.⁵⁴ The parameters were also well below the charge per phase threshold of 4 nC/phase that more accurately characterizes the tissue-damaging effect when stimulating microelectrodes as suggested by previous studies.^{32,33} These results demonstrated that StimNET elicited robust, long-lasting, chronically stable behavioral detections at markedly low charge injections.

In one of the animals (mouse 3), during voltage transient measurement, a large direct current (DC), estimated to be 40 μA , was accidentally delivered for a few seconds. This current and duration are often used to create electrolytic lesions in the tissue.³⁰ This incident immediately drove up the detection thresholds of all contacts in L4–L6 that had been stable for 99 days with the mean threshold at 4.45 ± 0.33 to $13.73 \mu\text{A}$ (Figure S5). The detection threshold then subsequently decreased over a period of 116 days and finally settled at $4.87 \pm 2.14 \mu\text{A}$, which was similar to the values prior to the incident. The change in detection threshold in this case was consistent with our hypothesis that tight tissue-electrode integration is responsible for the low threshold we obtained. It can be explained as the large DC current we accidentally delivered damaging the local tissue, which increased the average distance from excitable neurons to the stimulation site, so that higher currents were required to elicit the same behavioral response. The tissue healed over time, which lowered the average distance from neurons to StimNET and the detection threshold with it.

StimNETs maintain tight tissue-electrode integration and normal function after chronic ICMS

We investigated the nature of the device-tissue interface by a combination of *in vivo* imaging and postmortem immunohistochemistry. Representative examples of *in vivo* 2P imaging acquired 2 months after implantation showed dense, healthy vascular networks surrounding and in close contact with the implanted StimNET. Populations of neurons co-resided within micrometers of the StimNET and the stimulating contacts with no signs of neuronal degeneration (Figure 5A). These observations are in qualitative agreement with the tight tissue-NET integration we reported previously without stimulation.^{36,41} To quantify the tissue response to the chronic implantation and stimulation of StimNET, we performed immunohistochemistry evaluations of the tissue surrounding StimNETs and compared between stimulating sites, passive (implanted but no stimulation) sites, and controls (contralateral hemisphere with no implantation) (Figure 5B). Fluorescence intensity of NeuN showed no changes with distance from StimNET, indicating the same neuronal density in the close vicinity of the StimNET as far away and as in the control. Fluorescence intensity of Iba-1 and GFAP had mild elevation within 50 μm of the StimNET, but there was no encapsulation of microglia or astrocytes (Figures 5B and 5C). Critically, there were no differences between the stimulating and the passive sites in any of these markers. These results suggest that StimNETs support the same stable, tightly integrated interface with brain tissue as the recording NETs, the tissue-device interface is drastically improved over the other rigid or less flexible electrodes,^{22–25} and the stimulating currents used in the study were within the safety limit and did not induce tissue damage.

Next, we investigated the functional integrity of StimNETs. Stimulation pulse number per animal was 4.7 million, 3.3 million, 2.4 million, 3.9 million, and 1.1 million (mice 1–5, respectively), with individual contact site pulse counts ranging from 12,000 to 1.9 million pulses. The longest performing animal (mouse 1 in the behavioral test) continued to behaviorally detect low-amplitude stimulation after 308 days of implantation until its backend connector failed, highlighting the longevity of StimNETs *in vivo*. We analyzed the impedance of StimNETs as a function of days post-implantation in the animals that underwent behavioral tests. Impedance of StimNET at 1 kHz from multiple animals showed stability over a chronic period of 37 weeks (260 days) (Figure 5D). This contrasts with previous studies that reported substantial increase or reduction in impedance during a long-term implantation period.^{17,29} The changes in impedance observed in other electrodes are attributed to biotic and abiotic failures at the tissue-device interface, such as glial scar encapsulation, damage of device insulation, corrosion, and delamination. The stable impedance we measured is consistent with the intact tissue interface we reported earlier, indicating that StimNETs were free of these biotic and abiotic failures. Furthermore, we repeatedly tested the charge injection capability over the chronic periods of experiments. Figure 5E shows voltage transients in response to 8 μA biphasic pulses from a representative contact at week 16 (day 114) and week 42 (day 293) post-implantation (week 0/day 0 and week 26/day 179 after the first behavioral test) that had output over 925,000 pulses. There were no significant changes in the waveform shape or amplitude, further highlighting the chronic device stability of StimNETs for a large amount of charge injections *in vivo*.

We assessed the recording quality longitudinally at the stimulation sites as an additional indication of the integrity of device and tissue-device interface, because both biotic and abiotic failures would result in degradation in recording quality. Figure 5F shows representative waveforms of spontaneous activity recorded by the same stimulation channel in each animal for chronic periods up to 42 weeks. After hundreds of thousands to nearly 2 million stimulation pulses, the StimNET contacts still captured high-amplitude waveforms without visible decay in signal amplitudes. To quantify the recording quality longitudinally, we deployed three commonly used metrics, peak-to-peak amplitude, noise level, and signal-to-noise ratio (SNR), each as a function of days post-implantation determined for all stimulation channels from a representative animal (mouse 2) (Figures 5G–5I). Throughout 280 days, the level of noise remained constant, and there was no observed decline in either peak-to-peak amplitude or SNR over time. The stable recording performance further supports that StimNETs maintained tight tissue-electrode integration and normal function after chronic ICMS.

DISCUSSION

Emerging neural electrode technology focusing on flexibility and miniaturization has made high-density, long-lasting, tissue-compatible neural recordings possible.^{34,35} It has been conceived that the same form factors that improved recording efficacy could also benefit stimulation.¹⁸ For example, carbon fiber electrodes coated with platinum-iridium could stimulate intracellularly and maintain stable impedances with cells over many hours.⁵⁵ However, it remained challenging to make these small and flexible electrodes structurally and functionally robust for long-term, *in vivo* stimulation. In this study, we engineered what are currently the thinnest, most flexible penetrating microelectrode arrays, StimNETs, for robust ICMS. Each microcontact on these devices stimulated up to 1.9 million pulses *in vivo* during 8 months of intracortical implantation without signs of biotic or abiotic failures. The number of stimulation pulses StimNETs output *in vivo* in this study was on par with the pulse number used in a recent human study of ICMS (each contact ranging from 170,000 to 4 million pulses) that had a longer period of implantation.¹⁷ These results suggested that StimNETs, with marked ultraflexibility and 1 μm total thickness, support long-term applications of ICMS.

We leveraged the integrated applications of *in vivo* imaging, behavioral, and histological techniques to decipher the spatial extent of neuronal activation, quantify the longitudinal behavioral detectability, and comprehensively characterize the tissue-electrode interface. Our application of multiple modalities stands out from previous studies, where most often a single modality was employed, and allows us to elucidate holistically the neuromodulation effects of StimNET-induced ICMS. We showed low thresholds of 1–2 μA both by Ca^{2+} imaging and by behavioral detection, longitudinal stability in the neuronal activation and high levels of spatial selectivity in time frames of a few months, and robust and stable behavioral detectability chronically up to 226 days at a record low current of 1.5 μA , with day-to-day variations as small as 1 μA maximum. Critically, the ultraflexibility of StimNETs, following the recovery of implantation damage during the first 2 weeks,^{36,41} permits intact tissue-electrode interface similar to that of recording NETs,^{36,37,41} including little neuronal loss, little glial encapsulation, and intact microvasculature with no bleeding.

The tight tissue integration of StimNETs is pivotal to superior stability and low threshold activation. Our approach provides an alternative path from current approaches of building more robust stimulators for large current stimulations. Instead, we pursue a distinct regime of low-current stimulation by tissue-integrated electrodes at little risk of interface deterioration or device abiotic failures from excessive charge injections.

In the stable phase of behavioral testing, the interday variations of median detectability in two animals (mouse 2 and 5) were at or smaller than 1 μA , which is the current resolution of the stimulator used in the experiment, demonstrating superior longitudinal stability of StimNETs. This stability is in stark contrast with previous studies using conventional electrodes that showed diverse variations over chronic applications of ICMS. For instance, a study using Neuronexus arrays in rats reported a decrease in detection threshold in the “learning phase” and an increase in the “chronic phase.” The magnitude of increase in threshold was potentially linked to the severity of foreign body response in a cortical-layer-dependent manner.³⁰ Another study using Utah arrays in a human patient showed little increase in detection threshold over a remarkable period of 1,500 days.¹⁷ However, the day-to-day variations in threshold were larger than 10 μA , about an order of magnitude larger than those observed in our study. Explantation analyses of the Utah arrays have shown evidence of material degradation, shank damage, and encapsulation for longer implants.^{28,29} A significant correlation was identified between stimulation and electrode damage.^{17,29} In our own experiment, an accidental application of large DC current that presumably induced local tissue damage resulted in an immediate elevation of detection threshold. All these results support our hypothesis that devices offering intimate tissue-electrode interface improve the focality, efficacy, and stability of ICMS and result in high-resolution, long-lasting, chronically stable neuromodulation without risking tissue damage.

Two-photon imaging has emerged as a powerful tool to decipher the neuronal response to ICMS at the single-cell resolution.^{20,43,44} Most previous studies were performed acutely (immediately after surgical procedures) and under anesthesia, which alters brain-wide neural activity, including network effects.⁵⁶ Rigid electrodes must be implanted at a large slant angle to accommodate the imaging objective, which may exacerbate the lasting neuronal process atrophy not only in the cortical depth dimension but also laterally along the cortical surface.⁵⁷ Ultraflexible StimNETs can conveniently deflect for a 90° turn under the cranial window, allowing for steep implantation angles that are decoupled from the orientation of the carrier chip. We investigated neural responses to ICMS 2 weeks or more after the implantation, at which time the surgical trauma had subsided.^{36,41} Importantly, we performed all experiments in awake mice and developed a unique image processing workflow to quantify ICMS-evoked activity from the background of spontaneous activity at a high throughput. These features allowed us to eliminate previous confounding factors and elucidate the spatial pattern of neuronal activation in the animal’s natural awake state at single-cell resolution, spanning sizable volumes, across various currents and over chronic periods. Our results at currents $\sim 7 \mu\text{A}$ showed similar, distributed activation of neurons compared with previous studies at similar^{20,43} and larger current levels,⁴⁴ which are consistent with neuronal activation of ICMS through the passage of axons.^{20,58} Notably, at very low currents (2 μA) that did not elicit responses in most previous studies, we identified a more focal activation than larger, more commonly tested currents. In addition, we uniquely

provided spatial selectivity measurements at the single-cell resolution for several weeks, supporting that the focal activation of neurons at low currents was longitudinally stable. These results highlight the importance of lowering the activation threshold to improve the spatial resolution and selectivity of ICMS for chronic applications.

Our work focuses on the implantable electrodes that make a direct interface with the nervous system. Therefore, StimNETs are compatible and could be integrated with orthogonal technological development focusing on miniaturized, wireless bioelectronics for stimulation, such as StimDust⁵⁹ and magnetoelectric implants.⁶⁰ The contact size used in this study was 24 μm in diameter, similar to what we developed previously for passive recording,^{36,45} and warrants detection of single-unit activity, as we demonstrated. While this study used single-shank, 32-channel devices, StimNETs are scalable, owing to the wafer-scale microfabrication including sputter deposition of IrO_x and high-throughput implantation we have developed.^{45,61} Furthermore, StimNETs have the same miniaturized form factors, particularly the thickness, as their recording counterparts, which permits implantation of many these devices at a high volumetric density.⁴⁵ Taken together, StimNETs provide a scalable, long-lasting, chronically stable, bidirectional interface with neurons at high spatial resolutions.

Limitations of the study

Although we clearly demonstrated that StimNETs elicited focal activation of a few neurons at a low current of 2 μA , the 2P imaging in our study spanned a cortical depth of only 400 μm , not able to reach L4–L6. Given the significant anatomical difference between shallow and deeper cortical layers, we cannot infer the activation pattern of deeper layers from the current study. Furthermore, we tailored the imaging acquisition and analysis to quantify the populational activation in a 3D volume at the single-cell resolution. Our approach compromised the temporal resolution and was insensitive to the subsecond dynamic response of neurons to stimulation.

STAR★METHODS

RESOURCE AVAILABILITY

Lead contact—Further information and requests for data and code should be directed to and will be fulfilled by the lead contact, Lan Luan (lan.luan@rice.edu).

Materials availability—This study did not generate new animal lines or unique reagents.

Data and code availability

- Access original data: All data reported in this paper will be shared by the lead contact upon request.
- Access original code: All original code may be obtained at publicly accessible GitHub repository at <https://github.com/XieLuanLab/StimNET>, <https://doi.org/10.5281/zenodo.7879485>.

- Access any additional information: Any additional information required to reanalyze the data reported in this paper is available from the lead contact upon request.

EXPERIMENTAL MODEL AND SUBJECT PARTICIPANT DETAILS

Animals—A total of 14 mice at least 8 weeks of age or older, $n = 9$ C57BL/6J-Tg(Thy1-GCaMP6s)GP4.3Dkim/J for 2P imaging experiments (4 male, 5 female), and $n = 5$ (3 mice of C57BL/6J (1 male, 2 female) and 2 of GCaMP6s (1 male, 1 female)) for behavioral experiments were bred on-site from breeding pairs acquired from Jackson Laboratories (Bar Harbor, ME) and used in the experiments. Mice were single housed following implantation of StimNETs in the Animal Resource facility at Rice University. 3 out of the imaging mice were excluded due to early occlusion of the cranial window and of breakage of backend connector. All surgical and experimental procedures in this study were in compliance with the National Institutes of Health Guidelines for the Care and Use of Laboratory Animals and were approved by the Rice University Institutional Animal Care and Use Committee.

METHOD DETAILS

StimNET fabrication—The 32-channel, single-thread StimNETs were fabricated by conventional photolithography and metallization on fused silica wafers using a multi-layer structure. Fused silica instead silicon was used as the substrate to reduce the photovoltaic effect in the substrate. The microfabrication procedure had the following steps. i) A nickel metal release layer was patterned by depositing 3nm Ti and 60nm Ni under the flexible section of the device. The use of sacrificial layer permits the application of planar photolithography for device fabrication. It also allows the flexible section of StimNETs to be fabricated together with the I/O interface that connect to external electronics for data amplification and transmission. ii) A bottom insulation layer was created by spin coating a diluted polyimide polymer (PI2574, HD Microchemicals) to reach ~500 nm thickness and baked in a vacuum oven at 350°C. iii) An interconnect layer was defined by photolithography and metallization of a 3nm Cr, 100nm Au, and 3nm Cr metal stack by electron (e)-beam evaporation (Sharon Vacuum Co., Brockton, MA). Additional layers of 3 nm Cr, 160 nm Ni, and 80 nm Au were deposited on the solder pads to increase the reliability of solder reflow and reduce alloying of solder and gold. iv) The top insulating layer was created in the same method as the bottom layer. v) The thread outline, via to the electrodes, and solder pads were defined by RIE etching (Oxford Instrument) using O_2/CF_4 gas mixture in the 9:1 ratio. vi) Microcontacts for recording and stimulation were defined by photolithography and sputter coating of 10nm Ti, 100 nm Pt, 10nm Ti, and 300nm IrO_x stack (AJA ATC Orion Sputter System). vii) A capping layer of 300 nm PI is defined and etched as described in previous steps. viii) Low-temperature solder balls were placed on solder pads to form a ball grid array using a solder jetting tool (PacTech), and the wafer was diced into individual devices. The maximum PI curing temperature was 350°C. The StimNETs were then individually bonded to a custom printed circuit board (PCB) to interface with recording/stimulation electronics. Then the flexible section of StimNETs was released from the substrate by etching of the Ni layer, and the glass substrate was cleaved to the desired length. Lastly, the flexible implantable portion of the StimNET was affixed to a

50- μm diameter sharpened tungsten wire via Polyethylene glycol (PEG), which served as a temporary adhesive securing the probe for implantation as previously described in detail.⁶⁶

Simulation of electric stimulations—Finite element (FE) model simulations of the electrical stimulation produced by StimNET electrodes were conducted in COMSOL Multiphysics 5.6 (COMSOL, Inc., Burlington, MA). StimNETs were modeled in COMSOL with dimensions matching those utilized in this study, implanted within the center of a uniform block ($1.5 \times 1.5 \times 3$ mm) of neural tissue. To evaluate the impact of a glial scar on stimulation efficacy, an encapsulating volume representing the glial scar of 0, 20 and 40 μm was used. The FE models contained between 14,414,413 and 14,564,731 elements depending on glial scar thickness, and used following electrical properties: electrode polyimide substrate, conductivity of $1\text{e-}12$ S/m and permittivity of 11.7⁶⁷; gold contact sites, conductivity $9.43\text{e}6$ S/m and permittivity of 2.7604⁶⁷; neural tissue, conductivity 0.2 S/m and permittivity of 88.9⁶⁸; glial scar, conductivity 0.166 S/m and permittivity of 88.9.⁶⁹

To quantify the population of neurons activated by monopolar stimulation, the stimulation microcontact was modeled as the current source and the outer boundaries of the model as the ground. The current injected through the source was varied, and the volume of activated tissue was measured to be the neuronal tissue, excluding the glial scar, that reached or exceeded a charge density threshold of $1292 \mu\text{A}/\text{mm}^2$ following values from ref. ⁷⁰. A density of neurons of 110,000 neurons/mm was used⁷¹ to quantify the number of neurons activated by this stimulation. The effect of glial scar thickness was examined by running the simulations with no glial scar element or including either a 20 or 40 μm thick scar.

To quantify the spatial selectivity of neuronal tissue activation, two neighboring contact sites with an inter-site distance of 60 μm (center-to-center) at varied stimulation currents and with glial scars of 0, 20, or 40 μm thick were modeled using the identical conditions as above. The volume of neuronal tissue activated from each contact independently was referred to as the ‘single electrode stimulated volume’, and the volume of activated neuronal tissue activated by both contact sites was referred to as the overlapping region.

***In vitro* characterization of StimNET**—The charge injection and storage capacity of StimNETs was evaluated by cyclic voltammetry (CV) and voltage transient measurements in saline using Gamry Reference 600+ (Gamry Instruments, Warminster, PA). Measurements were made in a three-electrode setup using a large-area platinum counter electrode and Ag/AgCl (3M NaCl) reference electrode (BASi Research Products, West Lafayette, IN). Voltage transients were measured in response to biphasic pulses with 100 μs pulse width, and 33 μs interphase interval of various amplitudes. The pulse width and interphase intervals were shorter than *in vivo* stimulation to speed up *in vitro* testing and to permit 50 million pulses within a reasonable time frame. CV measurements used a sweep rate of 100 mV/s and were swept between 0.8V and -0.6V.

Surgical procedure—All animals received co-implantation of a cranial optical window and StimNET in one surgery.⁶⁶ Briefly, animals were anesthetized with isoflurane (3% for induction and 1%–2% for maintenance) and administered extended-release Buprenorphine (Ethiqva TM) and Dexamethasone (2 mg/kg, SC) for analgesia and to reduce surgery-induced

inflammation, respectively. The surgical site was infiltrated with lidocaine (7 mg/kg 0.05%) subcutaneously prior to shaving and disinfected with 3× iodine and alcohol wash before the initial incision into the skin of the head. The skull was exposed between bregma and lambda skull sutures, followed by the removal of the fascia and scoring of the skull crosshatch pattern to prepare the skull. A circular craniotomy of dimensions 3mm in diameter over the somatosensory cortex was drilled in the skull for the StimNET implantation, and a burr hole was drilled in the contralateral hemisphere to accommodate a Type 316 stainless steel grounding wire. Following the opening of the craniotomy, a 32-contact StimNET affixed to a 75 mm tungsten wire via the bio-dissolvable adhesive PEG was implanted through the dura to the somatosensory cortex by stereotaxic targeting at approximately 2 mm ML and -1.5 mm AP at an insertion angle of 30 degrees off vertical, though variations in exact position were made to accommodate surface vasculature and ensure a clear region in the vicinity of the probe implantation site to permit imaging. Following the implantation of the StimNET, the PEG affixing the StimNET to the shuttle wire was allowed to dissolve, and the wire was removed. A sterile glass coverslip window (#1, manufacturer) was secured over the craniotomy using cyanoacrylate adhesive and Metabond dental cement (Parkell, NY) with regions not directly covered by glass filled with Kwiksil (World Precision Instruments). Additional dental cement was applied to adhere a headbar for head fixation to the skull cap and seal the cranial window to the skull. Animals were provided at least three days of recovery post-surgery and an additional three days of familiarization to head restraint before the beginning of any experiments. The depth of implantation was targeted via stereotaxic linear drive. The insertion was prompt to prevent pre-mature detachment between PEG and StimNETs. Our previous study showed that this method had a target accuracy of 55 μm in depth in mouse neocortices.⁶¹

Two-photon imaging—Two-photon (2P) imaging was performed using a laser scanning microscope (Ultima 2p plus Bruker, MA) equipped with a 16× water immersion objective (numerical aperture of 0.8, Nikon, NY) and an ultrafast laser tuned to 920 nm for fluorescence Ca^{2+} excitations (InSight X3, Spectra-Physics). After initial habituation, z stack 2P imaging was performed, for which mice were awake and head-restrained on a home-constructed low-friction rodent-driven belt treadmill following the design of HHMI Janelia (<https://www.janelia.org/open-science/low-friction-rodent-driven-belt-treadmill>). Each imaging session lasted up to 3 h and contained multiple replicants. Each replicant contained alternating stimulation and baseline (no stimulation) trials from randomized stimulation sites and currents. Images (512×512 pixels) over a field of view up to 1 mm \times 1 mm were acquired at 30 fps using galvo-resonant scanners. The duration of a typical z stack, referred to as an imaging trial, was 26.98 s for a depth of 400 μm at the z-spacing of 2 μm (200 images at four frame averaging). Electrical stimulation was continually provided via a custom Pico32+Stim front end with a Grapevine neural interface processor (Ripple Neuro, Salt Lake City, UT) to sustain the neuronal activation during the entire imaging trial, which allows for quantification of population activation throughout the z stack. An inter-trial period of 2–5 s was implemented for data saving. 50 Hz electrical stimulation pulse trains of biphasic, charge-balanced cathode-leading square pulses at 167 μs per phase and 67 μs inter-phase interval were provided in 400 ms bursts per second for the duration of the imaging period. We chose 50 Hz for imaging to elicit relatively fast

rise in Ca^{2+} fluorescence.⁴² The current amplitudes were 2, 5, 7, and 10 μA , resulting in a maximum charge injection of 1.67 nC/ph per phase and a maximum charge density of 369.5 $\mu\text{C}/\text{cm}^2$. According to the Shannon criteria, the largest stimulation current gave a $K = 0.48$, smaller than the threshold of 1.85 for tissue compatible/safe neural stimulation. Customized MATLAB (MathWorks, MA) scripts were developed to randomize stimulation parameters and control data acquisition. Stimulation and 2P imaging were synchronized via TTL signals generated by a PulsePal (Sanworks, NY) unit.

Identification of stimulation-induced Ca^{2+} neural activation—2P imaging data were processed using a custom-written program integrating MATLAB (MathWorks, MA) and ImageJ⁷² to identify and isolate neurons activated by neural stimulation from the background (Figure 2D). The first goal is to identify regions of interest representing activated neurons in an imaging session. First, the voxel-by-voxel value of fluorescence intensity and standard deviation (STD) was calculated for all the baseline (no stimulation) trials during an imaging session, which provided a quantification of the spontaneous (passive) neural activity of the brain. Next, the stimulation-induced fluorescence increase was determined by subtracting baseline fluorescence from stimulation trials voxel by voxel. The baseline fluorescence was determined by averaging six baseline trials temporally proximal to the stimulation trial, the three prior and three after, to minimize the variability in individual baseline scans. The stimulation-induced activation was then determined as binarized voxels at a threshold of stimulation-induced fluorescence increase greater than three times the STD of the baseline fluorescence. These steps were performed for all stimulation trials, and the regions of stimulation-induced activations were summed across all trials to generate the voxel-by-voxel map containing all regions of activation that were weighted by the number of trials of activation. Finally, all regions of activation were segmented by the ImageJ plugin ‘3D iterative segmentation’⁶⁵ to provide regions of interest (ROIs) that defined neurons activated throughout the entire imaging session across stimulation sites and currents.

The next goal is to identify neurons activated by a particular stimulation parameter. First, randomized stimulation scans were regrouped by stimulation sites and currents. For each stimulation parameter, the same differential calculation as described above was repeated to obtain maps of stimulation-induced fluorescence increase, which was then masked by the segmented ROIs obtained previously and binarized by the same threshold as previously discussed to obtain stimulation-activated neuron ROIs. Then consistency of activation was checked across N trials under identical stimulation parameters, and ROIs consistently activated by more than 75% were marked as stimulation-activated neurons.

Quantification of neuronal activation via 2P imaging—To evaluate the neuronal response to ICMS, several metrics were quantified after the identification of activated neurons by 2P imaging, including the number of activated neurons, the consistency of activated neurons, the distance of neural activation, the density of activation, and the spatial specificity of stimulation. Calculating the number of activated neurons for a given stimulation current or population was accomplished by simply summing the total number of activated neuron ROIs detected. To quantify the fraction of neurons activated at low

currents that was also activated at higher current, we spatially tracked the individual neuron ROIs from a lower stimulation current to the next higher level (e.g., 2 μA –5 μA), identified neurons activated by both currents, counted their number, and divide it by the number of total number of neurons activated at the low current.

The maximum three-dimensional neural activation distance from the stimulating contact site was considered the maximum Cartesian distance between the centroid of an activated neuron and the stimulating contact site. The activation density was calculated as the number of activated neurons detected within 100- μm thick spherical shell bins emanating radially from the stimulating stimulation divided by the volume of the shell within the imaging volume (Figure S1). The spatial selectivity of activation was calculated by comparing the populations of neurons activated by two nearby sites within the same imaging session.

$$\text{SpatialSpecificity} = 1 - \frac{\text{Number of Neurons Activated by Both Contact Sites A AND B}}{\text{Number of Neurons Activated by Contacts Sites A OR B}}$$

Spatial specificity was evaluated for contact sites spaced 60, 120, and 180 μm apart and across all stimulation current levels.

Behavioral training—After a post-surgical recovery period of 7 days, the animals undergoing behavioral testing were put on water restriction Monday through Friday and on ad libitum water during the weekends and holidays. The animals were monitored every weekday to ensure their weights were above 85% of baseline body weight. Every animal received a minimum of 1 mL per weekday. If the animal did not receive all its daily allotment of water during the behavioral task, the remainder of its daily allotment was given after an hour had passed following the end of the behavioral session. Behavioral testing was performed using a standardized experimental rig from the International Brain Laboratory⁶⁴ with the following customizations. To accommodate electronics and cabling of StimNET, custom-fabricated headbar holders were used. The wheel for decision making was oriented 90° such that the wheel could be spun forwards and backward rather than left and right, allowing for a more natural movement for a go/no-go task. Electrical stimulation was delivered via a Pico32+Stim front end customized for small current output with a Grapevine Neural Interface Processor (Ripple Neuro, Salt Lake City, UT) onto StimNET sites that had impedance <1 M Ω at 1 kHz. All microstimulation was performed using cathode-leading pulses with a pulse width of 167 μs and 67 μs interphase interval, which was chosen to optimize percepts while minimizing currents.¹⁴ The frequency of stimulation was maintained at 100 Hz for longitudinal threshold measurements, a stimulation frequency commonly used in human ICMS experiments.¹⁷ For charge per second minimization experiments, a sweep of stimulation frequencies from 5 to 100 Hz was performed. The stimulation and recording were controlled via Xippmex MATLAB application programming interface (The MathWorks Inc., Natick, MA) on a computer separate from the behavioral task controlling computer.

The behavior training had two stages after acclimation to handling and head fixation. At Stage 0, the animal freely turned the wheel without stimuli and obtained a water reward

(10% sucrose solution) for wheel-turning behavior every trial passing an angular threshold. The initial angular threshold started at 20° and increased with sessions and response rate to a final value of 30°. The animal graduated stage 0 training once the response rate exceeded 95%. The purpose of this stage was to shape goal-directed behavior by forming a response-outcome association between the wheel turn and sugar water. Stage 1 introduced single-site suprathreshold (15 μ A) ICMS as the stimulus and the response-outcome association was made contingent upon the stimulus to form a stimulus-response-outcome chain. At this stage, the animal was rewarded by turning the wheel past the angular threshold (i.e., a Go response) during a response period beginning after the stimulus. The response period had an initial duration of 10 s and was concurrent with a 10 s stimulus. A Go response during the response period resulted in extinguishing the stimulus and reward delivery. If the animal did not respond within the response period, there was no penalty. Each trial was followed by an intertrial interval (ITI). The ITI was randomized and drawn from a uniform distribution with an initial interval of 2–3 s. The trial began with a pre-stimulus period (PSP) of 0.5 s to discourage premature responses. Responses during the PSP were negatively reinforced by resetting PSP, which delayed the stimulus and thus delayed opportunity to receive reward. If the animal appeared to respond well to the suprathreshold stimulation with PSP violation rate less than 30% of trials, the response period was decreased incrementally (1–2 s) over multiple sessions to a final period of 1 s. Similarly, the ITI upper bound was incrementally increased (0.5–1 s) to 6 s such that the final ITI was drawn from a uniform distribution with an interval of 2–6 s. PSP was incrementally increased (0.2–0.3 s) to a final value of 1.5 s. If the animal did not respond to stimulation, the animal was given one more session stimulation before another site was chosen. After the animal was able to produce consistent low latency responses within 1 s with a low PSP violation rate (<10% of trials), the animal graduated training and advanced to detection threshold measurements. Animals typically needed 2 weeks of training to proceed to detection threshold measurements.

ICMS threshold detection—To measure the ICMS detection thresholds across multiple contact sites and animals efficiently, an adaptive staircase procedure was employed.^{46,47} This procedure was run for each of the viable stimulation sites in a randomized manner. For a given trial, if the animal responded to the stimulus, the current for the subsequent trial was decreased by a step of 1 μ A. However, if there was no response, the current for the next trial was increased by a step of 1 μ A. The staircase procedure terminated if it did not respond to the maximum current (25 μ A) trials three consecutive times, the number of trials exceeded 25 trials, or after nine reversals where a reversal is defined as the transition from an increasing or decreasing trend to a subsequent decreasing or increasing trend, respectively. The threshold was the average of the last four reversals. The initial step size was 3 μ A and changed to 1 μ A after the third reversal.

***In vivo* electrophysiology**—Voltage transients were measured with respect to a Type 316 stainless steel reference wire. Voltage transient measurements were performed weekly on behavioral animals using the chronopotentiometry function on the Gamry Reference 600+ (Gamry Instruments, Warminster, PA) to assess the charge injection capacity of the stimulating electrodes. The input current waveform was a cathode-leading biphasic charge-balanced pulse with a pulse width of 167 μ s and 67 μ s interphase interval with

an amplitude of 8 μ A. The maximum cathodically and anodically driven electrochemical potential excursions (E_{MC}) were measured as the potential 20 μ s after the end of the cathodic and anodic phases, respectively.

In vivo impedance measurements at 1 kHz were performed weekly on animals using an Intan RHS stim/recording controller and RHS 32-channel stim/recording headstage (Intan Technologies, Los Angeles, CA). Contact sites which report impedances over 3 Mohm are considered to have a broken backend connection and removed from subsequent impedance measures. The average yield of fully functional contacts was 90%. Neural electrophysiological recording was performed on the animals under behavioral experiments using Intan or Ripple. To remove the confounding effect of stimulation on spiking activity within a session, we analyzed the first minute of each recording where there were few or no stimulation pulses. Any stimulation pulses found were removed by blanking. The resulting data was then common average referenced and bandpass filtered with lower and upper cutoff frequencies of 300 and 5000 Hz, respectively. Spike detection was performed on each stimulation channel using the MATLAB command “findpeaks”. Since “findpeaks” looks for positive-valued peaks, the sign of the input signal was flipped. The threshold value was set to $4.5 \times V_{rms}$ of the preprocessed filtered signal. The minimum distance between peaks was set to 1.5 ms. Additionally, the “halfprom” minimum peak prominence, maximum peak width, and minimum peak width were set to 40 μ V, 25 samples (0.8 ms), and 5 samples (0.167 ms), respectively. Spike waveforms were obtained by taking 10 samples before the threshold crossing and 38 at and after. Principal component analysis (PCA) of the waveform and K-means clustering were subsequently performed. Clusters had to have at least 60 events corresponding to a minimum average firing rate of 1 Hz. If more than one cluster on a channel was found, the largest amplitude cluster was selected to represent that channel. Noise level was quantified as the median average deviation (MAD) \times 1.4286 of that channel’s baseline recording and the signal-to-noise ratio (SNR) as the ratio of the maximum amplitude of the average waveform on each channel divided by that channel’s noise.

Histological tissue collection, *in situ* capture of StimNET, and analysis—For animals implanted for more than three months, brain tissue was collected and processed to quantify the chronic immune response to implanted StimNETs. For perfusion and tissue collection, animals were first anesthetized with isoflurane (3%–5%) and perfused PBS transcardially at 80 mmHg through the circulatory system of the animal until outflow was clear, followed by a fixative solution of roughly 500 mL 4% paraformaldehyde; both fluids were chilled to 4°C. Following perfusion, the head was removed from the body, burr holes were drilled throughout the skull to improve fluid flow, and the head was placed in a 4% paraformaldehyde solution for 48 h at 4°C for fixation. Afterward, the heads were cryoprotected by immersion in a 10% sucrose solution for 72 h and then frozen at -80°C for at least 24 h before extracting the brain from the skull. Care was taken to ensure the implanted electrode was not mechanically disturbed during the skull extraction. The frozen brains were then cryosectioned at 20 μ m thick with the electrode captured *in situ* via cryostat (CM1520 Leica Biosystems, IL), and slices were transferred to 48-well cell culture plates for fluorescence labeling.

Tissue slices were prepared for histology by first rinsing tissue three times in a 1× PBS solution with 0.1% Triton X-100 for 5 min each before blocking tissue in a 10% BSA solution for 1 h with gentle agitation at room temperature. Slices were then incubated with primary antibodies for neurons with conjugated mouse anti-NeuN (1:100 dilution, MAB377X; Millipore), microglia with chicken anti-GFAP (1:5000 dilution, ab134436; Abcam), and astrocytes with conjugated rabbit anti-Iba1 (1:1550 dilution, 015–28011; Fujifilm) in a solution containing 1% BSA overnight at 4°C. Slices were again rinsed three times in a 1× PBS solution with 0.1% Triton X-100 for 10 min each before being incubated in secondary antibody Goat Anti-Chicken Alexa Fluor 647(1:200 dilution, ab150171; Abcam) for 1 h at 4°C. Slices were washed three more times in a 1× PBS solution for 5 min periods before being sealed with Vectashield plus antifade mounting medium (Vector Laboratories, CA) doped with DAPI. Slides were placed in a dark chamber at 4°C for at least 24 h before imaging.

Confocal imaging of brain slices was performed with a Nikon A1 confocal microscope (Nikon Instruments Inc., Melville, NY). Four fluorescent channels were imaged to quantify the tissue response of neurons (488 nm), microglia (641 nm), astrocytes (561 nm), and cellular nuclei (405 nm). To quantify fluorescence intensity as a function of distance from StimNET, the boundary of StimNET in each tissue section were manually outlined. Then a custom analysis script written in ImageJ⁶² and MATLAB (MathWorks, MA) defined contours every 40 μm from 0 to 360 μm from the StimNET boundary. For each fluorescence channel, the average fluorescence in areas between every two adjacent contours was calculated as the intensity at that distance away from StimNET and normalized against the average fluorescent intensity in areas of 280–360 μm away from StimNET.

QUANTIFICATION AND STATISTICAL ANALYSIS

All statistical analyses were performed in MATLAB (MathWorks, MA). Results and details of the statistical comparisons performed in the study including sample sizes were reported in the results section and figure legends. In this study $p < 0.05$ was accepted as statistically different. Kruskal-Wallis tests with Dunn's post-hoc were used to compare the population of activated neurons by stimulation current with comparison of the distance of neural activation by stimulation current, the selectivity of stimulation at varied currents and distances, and the detection threshold of stimulation across cortical layers. Kruskal-Wallis tests with Dunn's post-hoc were employed for the comparisons at each binned distance for the histological evaluation of tissue neighboring stimulating, passive, and control contact sites.

Supplementary Material

Refer to Web version on PubMed Central for supplementary material.

ACKNOWLEDGMENTS

We thank Dr. Kevin Otto for helpful discussions, H. Rathore and Y. Jin for assistance with 2P imaging, Dr. Sonia Villapol for advice with histological preparation, Dr. A. Budi Utama at Rice SEA for assistance with histological imaging, the Animal Resource Facility at Rice University for animal care and housing, and the Rice nanofabrication facility for support on the microfabrication of StimNET. This work was funded by the National Institute of Neurological Disorders and Stroke, under R01NS109361 (to L.L.), R01NS102917 (to C.X.), and U01 NS115588

(to C.X.); by the Helsinki Institute of Life Science (N.T.), Academy of Finland (N.T.), and Fulbright Finland Foundation (N.T.); and by Rice University internal funds (L.L. and C.X.).

INCLUSION AND DIVERSITY

We worked to ensure sex balance in the selection of non-human subjects. One or more of the authors of this paper self-identifies as an underrepresented ethnic minority in their field of research or within their geographical location. One or more of the authors of this paper self-identifies as a gender minority in their field of research. One or more of the authors of this paper received support from a program designed to increase minority representation in their field of research. While citing references scientifically relevant for this work, we also actively worked to promote gender balance in our reference list.

REFERENCES

1. Penfield W, and Boldrey E (1937). Somatic motor and sensory representation in the cerebral cortex of man as studied by electrical stimulation. *Brain* 60, 389–443. 10.1093/brain/60.4.389.
2. Fritsch G, and Hitzig E (2009). Electric excitability of the cerebrum (Überdie elektrische Erregbarkeit des Grosshirns). *Epilepsy Behav.* 15, 123–130. 10.1016/j.yebeh.2009.03.001. [PubMed: 19457461]
3. Asanuma H, and Sakata H (1967). Functional organization of a cortical efferent system examined with focal depth stimulation in cats. *J. Neurophysiol.* 30, 35–54. 10.1152/jn.1967.30.1.35.
4. Stoney SD, Thompson WD, and Asanuma H (1968). Excitation of pyramidal tract cells by intracortical microstimulation: effective extent of stimulating current. *J. Neurophysiol.* 31, 659–669. [PubMed: 5711137]
5. Otto KJ, Rousche PJ, and Kipke DR (2005). Microstimulation in auditory cortex provides a substrate for detailed behaviors. *Hear. Res.* 210, 112–117. 10.1016/j.heares.2005.08.004. [PubMed: 16209915]
6. Ekstrom LB, Roelfsema PR, Arsenault JT, Bonmassar G, and Vanduffel W (2008). Bottom-up dependent gating of frontal signals in early visual cortex. *Science* 321, 414–417. 10.1126/science.1153276. [PubMed: 18635806]
7. Venkatraman S, and Carmena JM (2011). Active sensing of target location encoded by cortical microstimulation. *IEEE Trans. Neural Syst. Rehabil. Eng.* 19, 317–324. 10.1109/TNSRE.2011.2117441. [PubMed: 21382769]
8. Tabot GA, Dammann JF, Berg JA, Tenore FV, Boback JL, Vogelstein RJ, and Bensmaia SJ (2013). Restoring the sense of touch with a prosthetic hand through a brain interface. *Proc. Natl. Acad. Sci. USA* 110, 18279–18284. 10.1073/pnas.1221113110. [PubMed: 24127595]
9. Gallistel CR, Shizgal P, and Yeomans JS (1981). A portrait of the substrate for self-stimulation. *Psychol. Rev.* 88, 228–273. [PubMed: 6264530]
10. Tehovnik EJ (1996). Electrical stimulation of neural tissue to evoke behavioral responses. *J. Neurosci. Methods* 65, 1–17. 10.1016/0165-0270(95)00131-x. [PubMed: 8815302]
11. Voigt MB, Yusuf PA, and Kral A (2018). Intracortical microstimulation modulates cortical induced responses. *J. Neurosci.* 38, 7774–7786. 10.1523/JNEUROSCI.0928-18.2018. [PubMed: 30054394]
12. Armenta Salas M, Bashford L, Kellis S, Jafari M, Jo H, Kramer D, Shanfield K, Pejsa K, Lee B, Liu CY, and Andersen RA (2018). Pro-prioceptive and cutaneous sensations in humans elicited by intracortical microstimulation. *Elife* 7, e32904. 10.7554/eLife.32904. [PubMed: 29633714]
13. Chen X, Wang F, Fernandez E, and Roelfsema PR (2020). Shape perception via a high-channel-count neuroprosthesis in monkey visual cortex. *Science* 370, 1191–1196. 10.1126/science.abd7435. [PubMed: 33273097]
14. Fernández E, Alfaro A, Soto-Sánchez C, Gonzalez-Lopez P, Lozano AM, Peña S, Grima MD, Rodil A, Gómez B, Chen X, et al. (2021). Visual percepts evoked with an intracortical 96-channel

- microelectrode array inserted in human occipital cortex. *J. Clin. Invest.* 131, e151331. 10.1172/JCI151331. [PubMed: 34665780]
15. Flesher SN, Collinger JL, Foldes ST, Weiss JM, Downey JE, Tyler-Kabara EC, Bensmaia SJ, Schwartz AB, Boninger ML, and Gaunt RA (2016). Intracortical microstimulation of human somatosensory cortex. *Sci. Transl. Med.* 8, 361ra141. 10.1126/scitranslmed.aaf8083.
 16. Schmidt E, Bak MJ, Hambrecht FT, Kufta CV, O'Rourke DK, and Vallabhanath P (1996). Feasibility of a visual prosthesis for the blind based on intracortical microstimulation of the visual cortex. *Brain* 119, 507–522. [PubMed: 8800945]
 17. Hughes CL, Flesher SN, Weiss JM, Downey JE, Boninger M, Collinger JL, and Gaunt RA (2021). Neural stimulation and recording performance in human sensorimotor cortex over 1500 days. *J. Neural. Eng.* 18, 045012. 10.1088/1741-2552/ac18ad.
 18. Pancrazio JJ, Deku F, Ghazavi A, Stiller AM, Rihani R, Frewin CL, Varner VD, Gardner TJ, and Cogan SF (2017). Thinking small: progress on microscale neurostimulation technology. *Neuromodulation* 20, 745–752. 10.1111/ner.12716. [PubMed: 29076214]
 19. Urdaneta ME, Koivuniemi AS, and Otto KJ (2017). Central nervous system microstimulation: towards selective micro-neuromodulation. *Curr. Opin. Biomed. Eng.* 4, 65–77.
 20. Histed MH, Bonin V, and Reid RC (2009). Direct activation of sparse, distributed populations of cortical neurons by electrical microstimulation. *Neuron* 63, 508–522. 10.1016/j.neuron.2009.07.016. [PubMed: 19709632]
 21. Butovas S, and Schwarz C (2003). Spatiotemporal effects of microstimulation in rat neocortex: a parametric study using multielectrode recordings. *J. Neurophysiol.* 90, 3024–3039. 10.1152/jn.00245.2003. [PubMed: 12878710]
 22. Polikov VS, Tresco PA, and Reichert WM (2005). Response of brain tissue to chronically implanted neural electrodes. *J. Neurosci. Methods* 148, 1–18. 10.1016/j.jneumeth.2005.08.015. [PubMed: 16198003]
 23. Grill WM, Norman SE, and Bellamkonda RV (2009). Implanted neural interfaces: biochallenges and engineered solutions. *Annu. Rev. Biomed. Eng.* 11, 1–24. 10.1146/annurev-bioeng-061008-124927. [PubMed: 19400710]
 24. Barrese JC, Rao N, Paroo K, Triebwasser C, Vargas-Irwin C, Franquemont L, and Donoghue JP (2013). Failure mode analysis of silicon-based intracortical microelectrode arrays in non-human primates. *J. Neural. Eng.* 10, 066014. 10.1088/1741-2560/10/6/066014. [PubMed: 24216311]
 25. Salatino JW, Ludwig KA, Kozai TDY, and Purcell EK (2017). Glial responses to implanted electrodes in the brain. *Nat. Biomed. Eng.* 1, 862–877. 10.1038/s41551-017-0154-1. [PubMed: 30505625]
 26. Davis TS, Parker RA, House PA, Bagley E, Wendelken S, Normann RA, and Greger B (2012). Spatial and temporal characteristics of V1 microstimulation during chronic implantation of a microelectrode array in a behaving macaque. *J. Neural. Eng.* 9, 065003. 10.1088/1741-2560/9/6/065003. [PubMed: 23186948]
 27. Koivuniemi A, Wilks SJ, Woolley AJ, and Otto KJ (2011). Multimodal, longitudinal assessment of intracortical microstimulation. *Prog. Brain Res.* 194, 131–144. 10.1016/B978-0-444-53815-4.00011-X. [PubMed: 21867800]
 28. Szymanski LJ, Kellis S, Liu CY, Jones KT, Andersen RA, Commins D, Lee B, McCreery DB, and Miller CA (2021). Neuropathological effects of chronically implanted, intracortical microelectrodes in a tetraplegic patient. *J. Neural. Eng.* 18, 0460b9. 10.1088/1741-2552/ac127e.
 29. Woeppel K, Hughes C, Herrera AJ, Eles JR, Tyler-Kabara EC, Gaunt RA, Collinger JL, and Cui XT (2021). Explant analysis of Utah electrode arrays implanted in human cortex for brain-computer-interfaces. *Front. Bioeng. Biotechnol.* 9, 759711. 10.3389/fbioe.2021.759711. [PubMed: 34950640]
 30. Urdaneta ME, Kunigk NG, Currin S, Delgado F, Fried SI, and Otto KJ (2022). The long-term stability of intracortical microstimulation and the foreign body response are layer dependent. *Front. Neurosci.* 16, 908858. 10.3389/fnins.2022.908858. [PubMed: 35769707]
 31. Cogan SF, Guzelian AA, Agnew WF, Yuen TGH, and McCreery DB (2004). Over-pulsing degrades activated iridium oxide films used for intracortical neural stimulation. *J. Neurosci. Methods* 137, 141–150. 10.1016/j.jneumeth.2004.02.019. [PubMed: 15262054]

32. McCreery DB, Agnew WF, and Bullara LA (2002). The effects of prolonged intracortical microstimulation on the excitability of pyramidal tract neurons in the cat. *Ann. Biomed. Eng.* 30, 107–119. 10.1114/1.1430748. [PubMed: 11874134]
33. McCreery D, Pikov V, and Troyk PR (2010). Neuronal loss due to prolonged controlled-current stimulation with chronically implanted microelectrodes in the cat cerebral cortex. *J. Neural. Eng.* 7, 036005. 10.1088/1741-2560/7/3/036005. [PubMed: 20460692]
34. He F, Lycke R, Ganji M, Xie C, and Luan L (2020). Ultraflexible neural electrodes for long-lasting intracortical recording. *iScience* 23, 101387. 10.1016/j.isci.2020.101387. [PubMed: 32745989]
35. Luan L, Robinson JT, Aazhang B, Chi T, Yang K, Li X, Rathore H, Singer A, Yellapantula S, Fan Y, et al. (2020). Recent advances in electrical neural interface engineering: minimal invasiveness, longevity, and scalability. *Neuron* 108, 302–321. 10.1016/j.neuron.2020.10.011. [PubMed: 33120025]
36. Luan L, Wei X, Zhao Z, Siegel JJ, Potnis O, Tuppen CA, Lin S, Kazmi S, Fowler RA, Holloway S, et al. (2017). Ultraflexible nanoelectronic probes form reliable, glial scar-free neural integration. *Sci. Adv.* 3, e1601966. 10.1126/sciadv.1601966. [PubMed: 28246640]
37. Wei X, Luan L, Zhao Z, Li X, Zhu H, Potnis O, and Xie C (2018). Nanofabricated ultraflexible electrode arrays for high-density intracortical recording. *Adv. Sci.* 5, 1700625. 10.1002/advs.201700625.
38. Slavcheva E, Vitushinsky R, Mokwa W, and Schnakenberg U (2004). Sputtered iridium oxide films as charge injection material for functional electrostimulation. *J. Electrochem. Soc.* 151, E226. 10.1149/1.1747881.
39. Cogan SF, Troyk PR, Ehrlich J, Plante TD, and Detlefsen DE (2006). Potential-biased, asymmetric waveforms for charge-injection with activated iridium oxide (AIROF) neural stimulation electrodes. *IEEE Trans. Biomed. Eng.* 53, 327–332. 10.1109/TBME.2005.862572. [PubMed: 16485762]
40. Maeng J, Chakraborty B, Geramifard N, Kang T, Rihani RT, Joshi-Imre A, and Cogan SF (2020). High-charge-capacity sputtered iridium oxide neural stimulation electrodes deposited using water vapor as a reactive plasma constituent. *J. Biomed. Mater. Res. B Appl. Biomater.* 108, 880–891. 10.1002/jbm.b.34442. [PubMed: 31353822]
41. He F, Sun Y, Jin Y, Yin R, Zhu H, Rathore H, Xie C, and Luan L (2022). Longitudinal neural and vascular recovery following ultraflexible neural electrode implantation in aged mice. *Biomaterials* 291, 121905. 10.1016/j.biomaterials.2022.121905. [PubMed: 36403326]
42. Michelson NJ, Eles JR, Vazquez AL, Ludwig KA, and Kozai TDY (2019). Calcium activation of cortical neurons by continuous electrical stimulation: frequency dependence, temporal fidelity, and activation density. *J. Neurosci. Res.* 97, 620–638. 10.1002/jnr.24370. [PubMed: 30585651]
43. Eles JR, Stieger KC, and Kozai TDY (2021). The temporal pattern of intracortical microstimulation pulses elicits distinct temporal and spatial recruitment of cortical neuropil and neurons. *J. Neural. Eng.* 18, 015001. 10.1088/1741-2552/abc29c.
44. Zheng XS, Yang Q, Vazquez A, and Cui XT (2022). Imaging the stability of chronic electrical microstimulation using electrodes coated with PEDOT/CNT and iridium oxide. *iScience* 25, 104539. 10.1016/j.isci.2022.104539. [PubMed: 35769881]
45. Zhao Z, Zhu H, Li X, Sun L, He F, Chung JE, Liu DF, Frank L, Luan L, and Xie C (2023). Ultraflexible electrode arrays for monthslong high-density electrophysiological mapping of thousands of neurons in rodents. *Nat. Biomed. Eng.* 7, 520–532. 10.1038/s41551-022-00941-y. [PubMed: 36192597]
46. Levitt H (1971). Transformed up-down methods in psychoacoustics. *J. Acoust. Soc. Am.* 49, 467+.
47. Koivuniemi AS, and Otto KJ (2011). Asymmetric versus symmetric pulses for cortical microstimulation. *IEEE Trans. Neural Syst. Rehabil. Eng.* 19, 468–476. 10.1109/TNSRE.2011.2166563. [PubMed: 21968793]
48. Callier T, Schluter EW, Tabot GA, Miller LE, Tenore FV, and Bensmaia SJ (2015). Long-term stability of sensitivity to intracortical microstimulation of somatosensory cortex. *J. Neural. Eng.* 12, 056010. 10.1088/1741-2560/12/5/056010. [PubMed: 26291448]
49. Ferroni CG, Maranesi M, Livi A, Lanzilotto M, and Bonini L (2017). Comparative performance of linear multielectrode probes and single-tip electrodes for intracortical microstimulation and single-

- neuron recording in macaque monkey. *Front. Syst. Neurosci.* 11, 84. 10.3389/fnsys.2017.00084. [PubMed: 29187815]
50. Ni AM, and Maunsell JHR (2010). Microstimulation reveals limits in detecting different signals from a local cortical region. *Curr. Biol.* 20, 824–828. 10.1016/j.cub.2010.02.065. [PubMed: 20381351]
 51. Sombeck JT, and Miller LE (2019). Short reaction times in response to multi-electrode intracortical microstimulation may provide a basis for rapid movement-related feedback. *J. Neural. Eng.* 17, 016013. 10.1088/1741-2552/ab5cf3. [PubMed: 31778982]
 52. Rousche PJ, and Normann RA (1999). Chronic intracortical microstimulation (ICMS) of cat sensory cortex using the Utah Intracortical Electrode Array. *IEEE Trans. Rehabil. Eng.* 7, 56–68. 10.1109/86.750552. [PubMed: 10188608]
 53. Urdaneta ME, Kunigk NG, Delgado F, Fried SI, and Otto KJ (2021). Layer-specific parameters of intracortical microstimulation of the somatosensory cortex. *J. Neural. Eng.* 18, 055007. 10.1088/1741-2552/abedde.
 54. Shannon RV (1992). A model of safe levels for electrical stimulation. *IEEE Trans. Biomed. Eng.* 39, 424–426. 10.1109/10.126616.
 55. Huan Y, Gill JP, Fritzingler JB, Patel PR, Richie JM, Della Valle E, Weiland JD, Chestek CA, and Chiel HJ (2021). Carbon fiber electrodes for intracellular recording and stimulation. *J. Neural. Eng.* 18, 066033. 10.1088/1741-2552/ac3dd7.
 56. Friedberg MH, Lee SM, and Ebner FF (1999). Modulation of receptive field properties of thalamic somatosensory neurons by the depth of anesthesia. *J. Neurophysiol.* 81, 2243–2252. 10.1152/jn.1999.81.5.2243. [PubMed: 10322063]
 57. Welle CG, Gao YR, Ye M, Lozzi A, Boretzky A, Abliz E, and Hammer DX (2020). Longitudinal neural and vascular structural dynamics produced by chronic microelectrode implantation. *Biomaterials* 238, 119831. 10.1016/j.biomaterials.2020.119831. [PubMed: 32045783]
 58. Kumaravelu K, Sombeck J, Miller LE, Bensaïma SJ, and Grill WM (2022). Stoney vs. Histed: quantifying the spatial effects of intracortical microstimulation. *Brain Stimul.* 15, 141–151. 10.1016/j.brs.2021.11.015. [PubMed: 34861412]
 59. Johnson BC, Shen K, Piech D, Ghanbari MM, Li KY, Neely R, Carmena JM, Maharbiz MM, and Muller R (2018). StimDust: a 6.5mm(3), wireless ultrasonic peripheral nerve stimulator with 82% peak chip efficiency. In *IEEE Custom Integrated Circuits Conference*.
 60. Chen JC, Kan P, Yu Z, Alrashdan F, Garcia R, Singer A, Lai CSE, Avants B, Crosby S, Li Z, et al. (2022). A wireless millimetric magnetolectric implant for the endovascular stimulation of peripheral nerves. *Nat. Biomed. Eng.* 6, 706–716. 10.1038/s41551-022-00873-7. [PubMed: 35361934]
 61. Zhao Z, Li X, He F, Wei X, Lin S, and Xie C (2019). Parallel, minimally-invasive implantation of ultra-flexible neural electrode arrays. *J. Neural. Eng.* 16, 035001. 10.1088/1741-2552/ab05b6. [PubMed: 30736013]
 62. Schneider CA, Rasband WS, and Eliceiri KW (2012). NIH Image to ImageJ: 25 years of image analysis. *Nat. Methods* 9, 671–675. 10.1038/nmeth.2089. [PubMed: 22930834]
 63. Sage D, Prodanov D, Tinevez J, and Schindelin J (2012). MIJ: Making Interoperability Between ImageJ and Matlab Possible. *ImageJ User & Developer Conference (Luxembourg)*, pp. 24–26.
 64. International Brain Laboratory; Aguillon-Rodriguez V, Angelaki D, Bayer H, Bonacchi N, Carandini M, Cazettes F, Chapuis G, Churchland AK, Dan Y, et al. (2021). Standardized and reproducible measurement of decision-making in mice. *Elife* 10, e63711. 10.7554/eLife.63711. [PubMed: 34011433]
 65. Ollion J, Cochenec J, Loll F, Escudé C, and Boudier T (2013). TANGO: a generic tool for high-throughput 3D image analysis for studying nuclear organization. *Bioinformatics* 29, 1840–1841. 10.1093/bioinformatics/btt276. [PubMed: 23681123]
 66. Yin R, Noble BC, He F, Zolotavin P, Rathore H, Jin Y, Sevilla N, Xie C, and Luan L (2022). Chronic co-implantation of ultraflexible neural electrodes and a cranial window. *Neurophotonics* 9, 032204. 10.1117/1.NPh.9.3.032204. [PubMed: 35036472]
 67. Serway RA (1998). *Principles of Physics, Second edition* (Saunders College Pub.).

68. Yousif N, Bayford R, and Liu X (2008). The influence of reactivity of the electrode-brain interface on the crossing electric current in therapeutic deep brain stimulation. *Neuroscience* 156, 597–606. 10.1016/j.neuroscience.2008.07.051. [PubMed: 18761058]
69. Malaga KA, Schroeder KE, Patel PR, Irwin ZT, Thompson DE, Nicole Bentley J, Lempka SF, Chestek CA, and Patil PG (2016). Data-driven model comparing the effects of glial scarring and interface interactions on chronic neural recordings in non-human primates. *J. Neural. Eng.* 13, 016010. 10.1088/1741-2560/13/1/016010. [PubMed: 26655972]
70. Tehovnik EJ, Tolia AS, Sultan F, Slocum WM, and Logothetis NK(2006). Direct and indirect activation of cortical neurons by electrical microstimulation. *J. Neurophysiol.* 96, 512–521. 10.1152/jn.00126.2006. [PubMed: 16835359]
71. Keller D, Erö C, and Markram H (2018). Cell densities in the mouse brain: a systematic Review. *Front. Neuroanat.* 12, 83. 10.3389/fnana.2018.00083. [PubMed: 30405363]
72. Schindelin J, Arganda-Carreras I, Frise E, Kaynig V, Longair M, Pietzsch T, Preibisch S, Rueden C, Saalfeld S, Schmid B, et al. (2012). Fiji: an open-source platform for biological-image analysis. *Nat. Methods* 9, 676–682. 10.1038/nmeth.2019. [PubMed: 22743772]

Highlights

- Ultraflexible electrode capable of robust charge injection and chronic stimulation
- Focal and spatially selective neural activation at a low current of 2 μ A
- Stable behavioral detectability for over 8 months at 0.25 nC/phase and lower
- Intact tissue-electrode interface with no neuronal degeneration or glial scarring

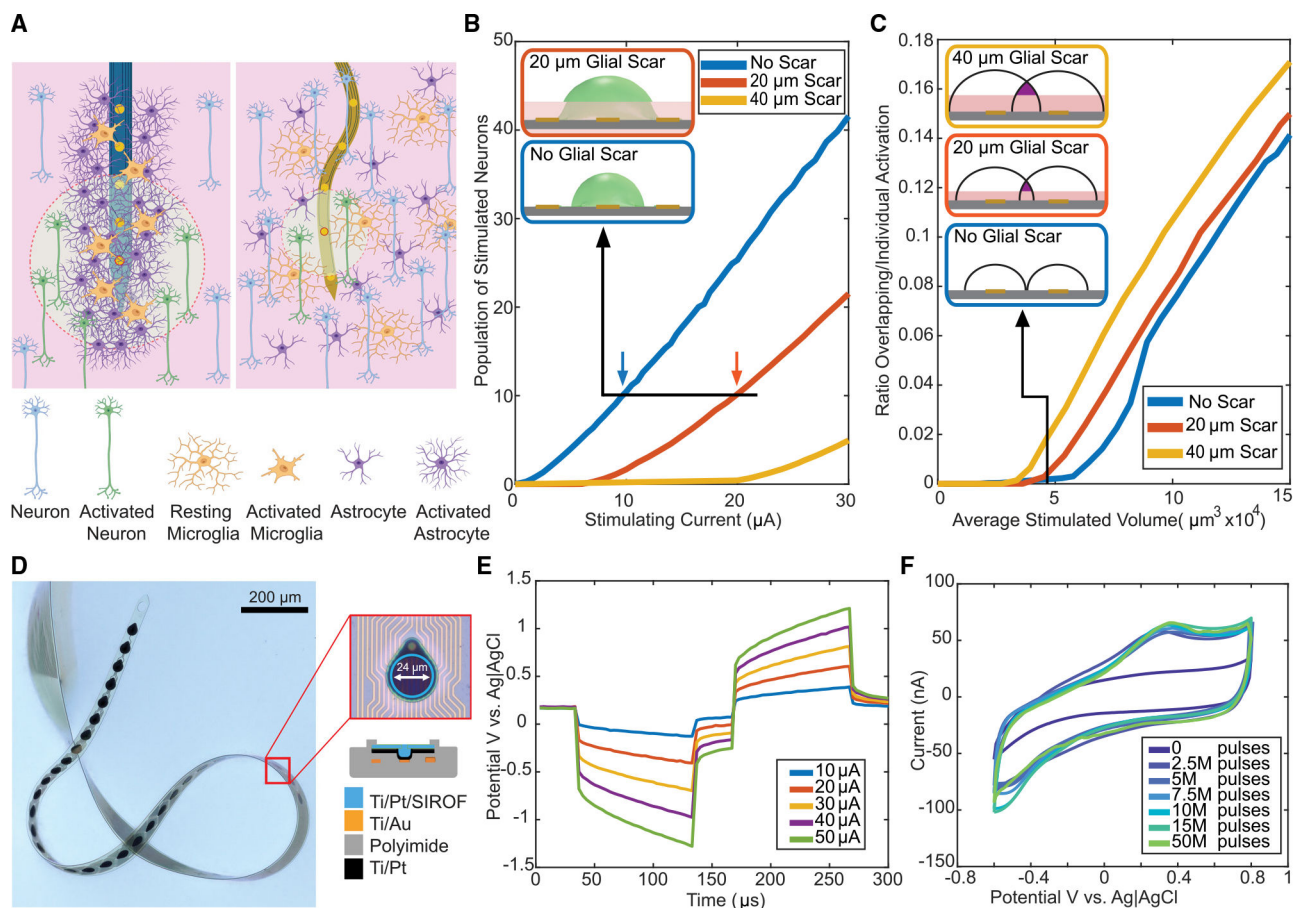


Figure 1. Engineering tissue-integrated flexible electrodes to enhance microstimulation efficacy

(A) Diagram of chronic immune response to rigid and flexible implants showing that, in theory, no glial scarring reduces the distance between the stimulation site and neurons so that a lower current can elicit more focal neural activation.

(B) Simulation showing that the current needed to activate the same number of neurons reduces with glial scar thickness. Inset: volume of activated neuronal tissue (shaded green) in the situation of no scar (bottom) and 20- μm -thick scar (top). Gray, polyimide; golden yellow, stimulation contacts; shaded pink, glial scar; shaded green, activated tissue volume. Arrows denote the stimulation currents in each case.

(C) Simulation showing that overlapping volume increases with scar thickness when stimulating two nearby sites. Inset: spatial profiles of the stimulated tissue volume when two stimulation sites activate the same volume where the scar thickness is 0, 20, and 40 μm . Black, outer boundary of activated tissue by each stimulation site; shaded purple, overlap of activation regions; shaded pink, glial scar.

(D) Photo of a meandering StimNET in water showing ultraflexibility. Inset: zoomed-in photo of a stimulation site and its cross-sectional structure. SIROF, sputter IrO_x film.

(E) Representative *in vitro* voltage transients at various current amplitudes.

(F) *In vitro* cyclic voltammograms at 100 mV/s showing stable charge storage capacity of a single contact after 50 million pulses at 30 μA .

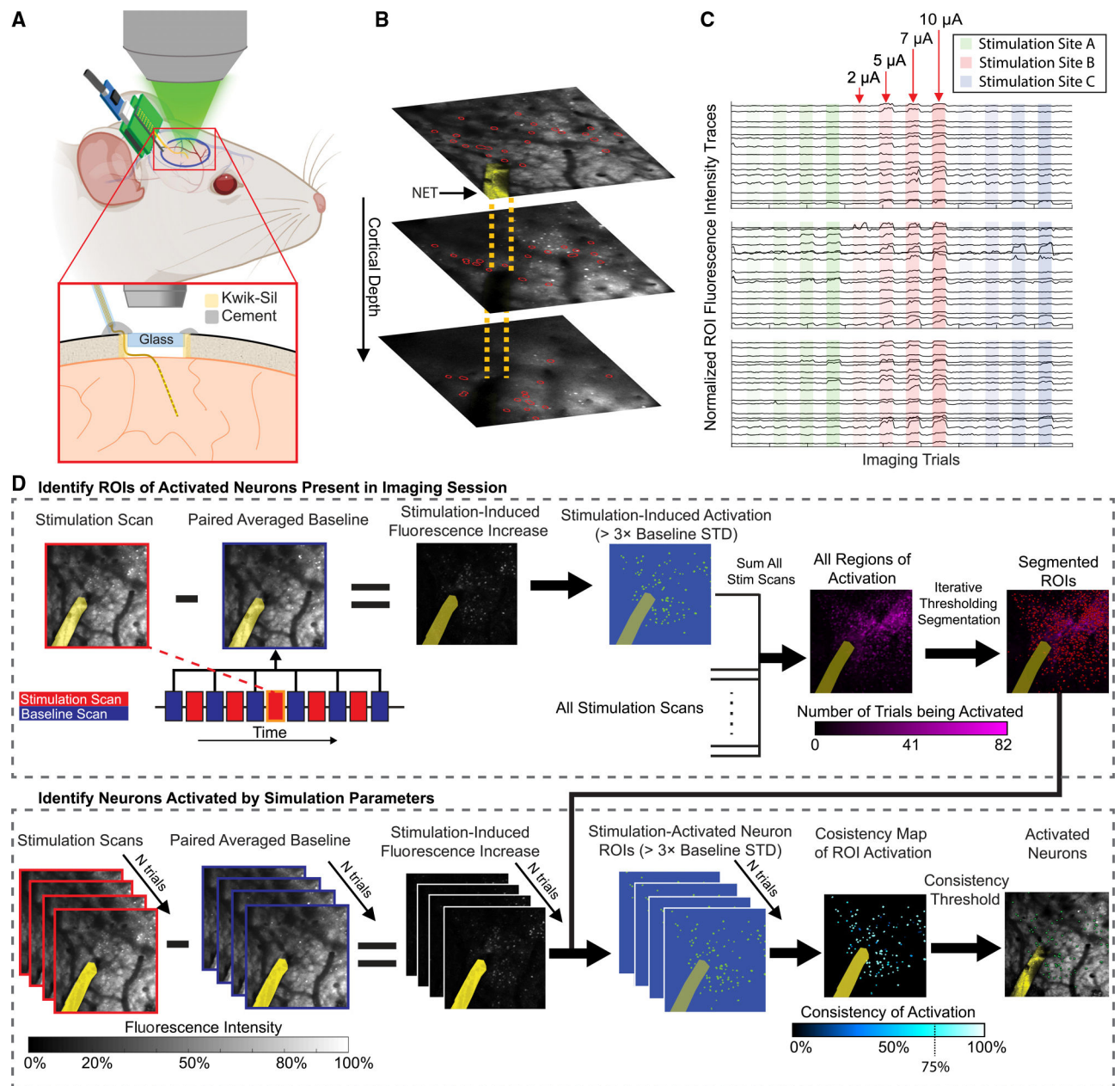


Figure 2. High-throughput quantification of ICMS-evoked neuronal activation in awake animals (A) Diagram illustrating the surgical preparation and experimental setup for synchronous two-photon Ca^{2+} neural imaging and ICMS in awake mice for longitudinal studies. (B) Representative Ca^{2+} images across the cortical depth during ICMS. Yellow ribbon and dashed lines, image and sketch of the StimNET. Red circles, representative neurons shown in (C). (C) Sample fluorescence intensity traces from neurons in (B) over multiple stimulation and baseline trials. A distinct subset of cells was activated by each stimulation site. (D) Image processing workflow to identify and localize neurons activated by ICMS in awake animals. Regions of interest (ROIs) for active neurons were identified by differential measurements of stimulated and non-stimulated trials, thresholded against

baseline fluorescence variance, and segmented for the entire imaging session. The segmentation results were then fed into the activation map of each stimulation parameter, which, after checking for consistency of activation >75% across repetitive trials, isolated the activated neurons by this specific stimulation parameter. Yellow ribbon, StimNET; red dots, neuron ROIs; green dots, evoked neurons.

Author Manuscript

Author Manuscript

Author Manuscript

Author Manuscript

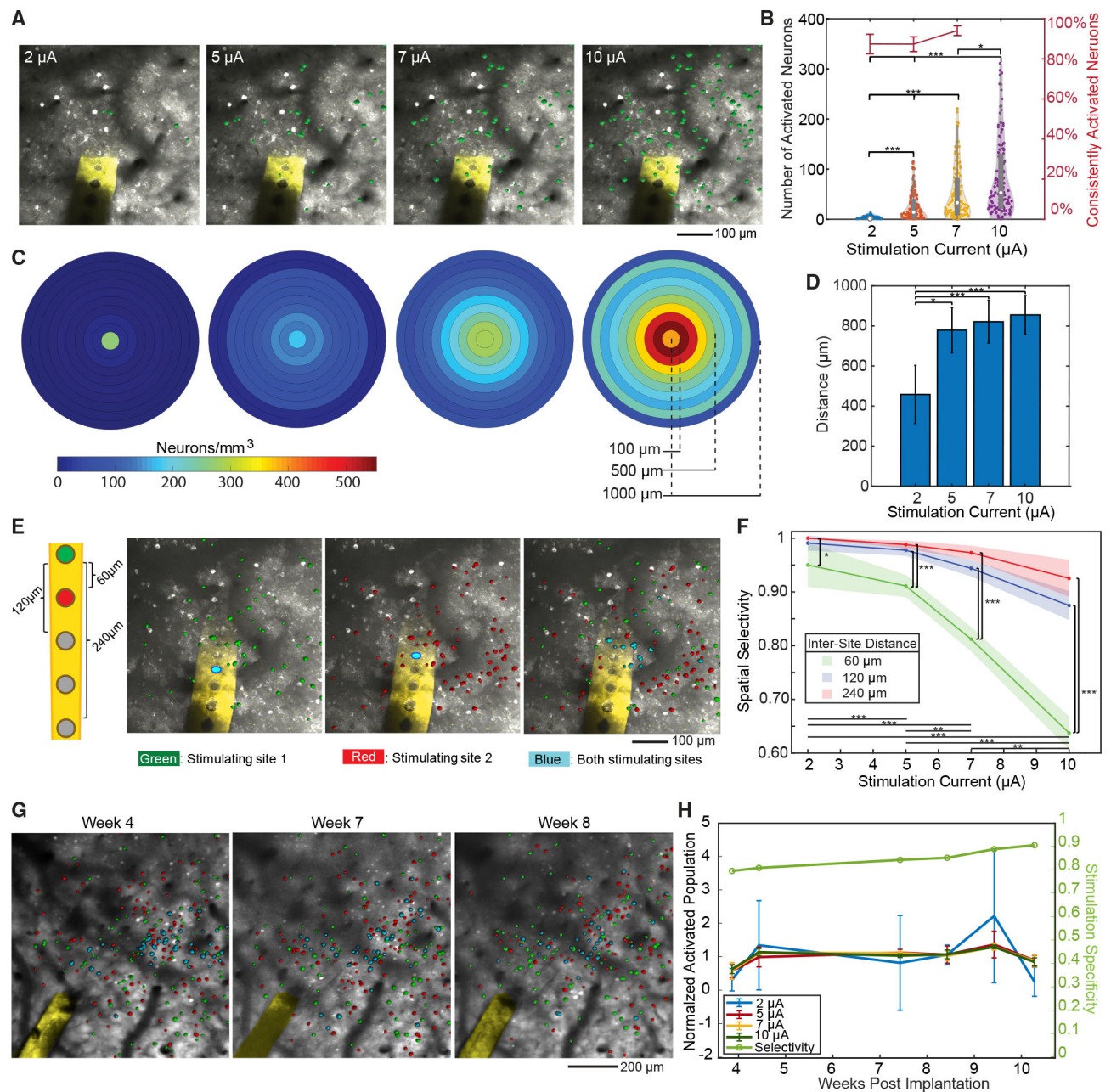


Figure 3. StimNET elicits spatially localized neuronal activation at low currents

(A) Representative 2P images showing neuronal activation increased with stimulation currents. Images are maximum-intensity projections (MIPs) of z stacks from 0 to 400 μm . Green, ICMS-evoked neurons; yellow, StimNET.

(B) Left axis: violin plot of total neural population activation. Embedded whisker plots denote the 25th, 50th, and 75th percentiles. Right axis: percentage of neurons being activated by the next higher current (Kruskal-Wallis test with Dunn's *post hoc* correction). Error bars denote 95% confidence intervals.

(C) Ring plots showing the averaged cell activation density as a function of distance in 3D from the stimulation sites.

(D) Bar plot of the maximum spatial spread of neural activation showing a significant increase from 2 μA to higher currents (Kruskal-Wallis test with Dunn's *post hoc* correction).

(E) Representative 2P MIPs of the same imaging volume showing adjacent stimulating sites at 5- μA -activated distinctive populations. Green, neurons activated by site 1; red, neurons activated by site 2; blue, neurons co-activated by sites 1 and 2. Sketch on the left shows the site separation.

(F) Spatial selectivity as a function of stimulation currents for three intersite separations (Kruskal-Wallis test with Dunn's *post hoc* correction).

(G) Representative 2P MIPs in the same animal showing consistent and spatially selective activation of neurons over time. Same color code as in (E). Center-to-center distance of two neighboring sites, 60 μm ; stimulation current, 7 μA .

(H) Normalized neural activation shows stable population recruitment over time (left axis). Error bars denote 95% confidence interval. Right axis displays the spatial selectivity over time at 5 μA . Sample numbers: $n = 5$ animals, 21 stimulation channels, and 11 imaging sessions for (B)–(D); $n = 6$ animals, 79 stimulation channels, and 20 imaging sessions for (F). $n = 3$ animals, 6 stimulation sites for (H). Statistical significance: * $p < 0.05$; ** $p < 0.01$; *** $p < 0.001$.

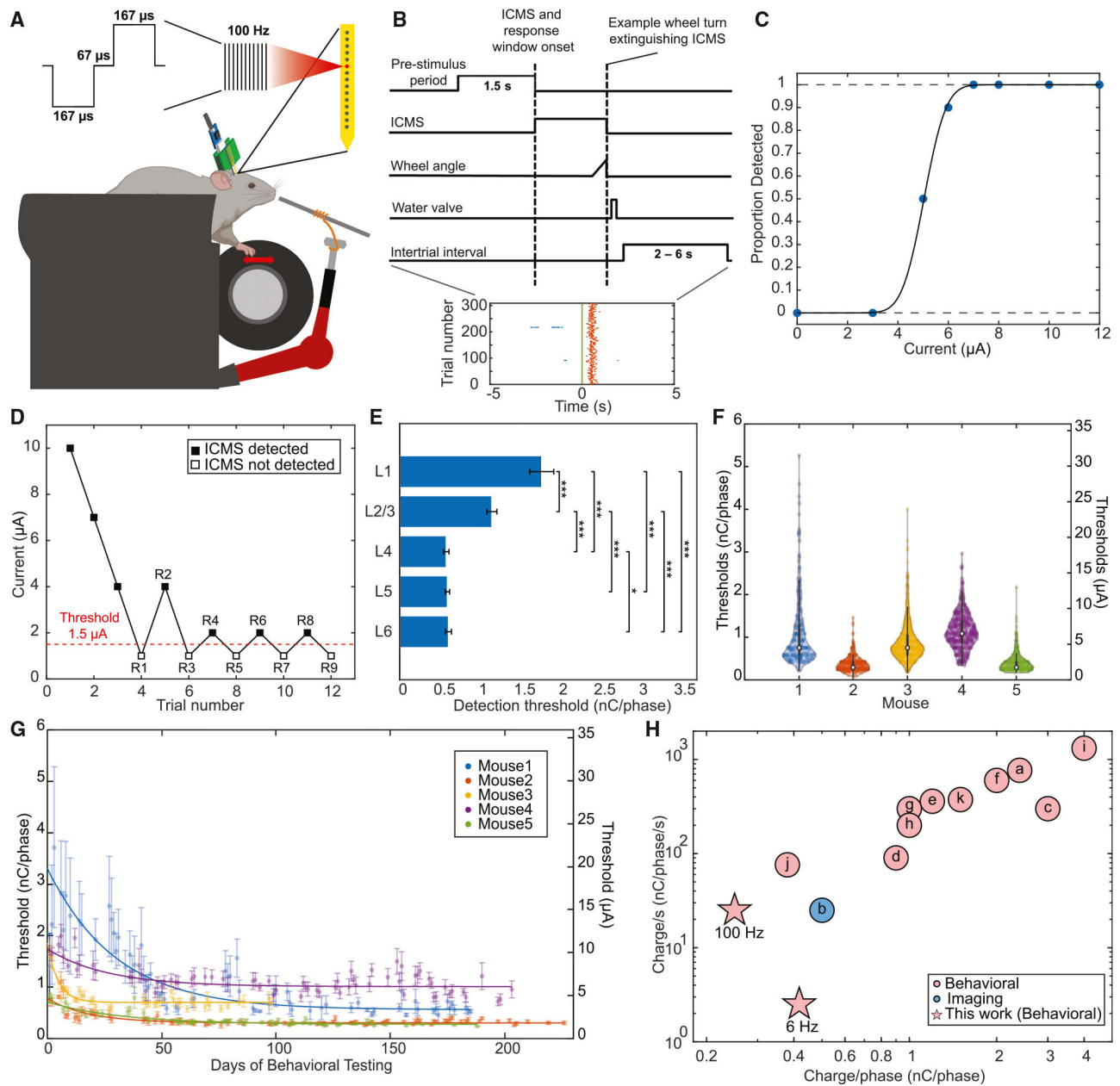


Figure 4. StimNETs elicit robust behavioral detection at low currents

(A) Sketch showing the wheel-turning task for ICMS behavioral detection. We used biphasic, cathode-leading pulses as depicted. The stimulation frequency was 100 Hz unless otherwise noted.

(B) Diagram of trial structure used for the go/no-go task. ICMS was used as both the only cue and the stimulus. Inset: response raster plot shows consistent, low latency response to suprathreshold stimulation (red dots) with very few impulsive turns in the pre-stimulation period (blue dots). $t = 0$ marks the onset of ICMS.

(C) Representative psychometric curve showing proportion of correct responses as a function of currents ($n = 1$ session, 80 trials).

(D) Representative threshold detection using adaptive staircase method. Threshold was calculated as the average of the last four reversals. Reversals are denoted as R1–R9.

(E) Detection thresholds at all cortical layers showing significant layer difference (Kruskal-Wallis test with Dunn's *post hoc* correction, *** $p < 0.001$, * $p < 0.05$). $n = 5$ animals, 64 stimulating contacts, and 362 sessions. Error bars denote 95% confidence intervals.

(F) Violin plot showing averaged detection thresholds within cortical layers 4–6 for all mice across all sessions. $n = 5$ animals, 38 stimulating contacts, and 362 sessions.

(G) Detection thresholds of all contacts in L4–L6 as a function of days showing lasting stability after initial decay. Solid lines are exponential fits. Error bars denote 67% confidence interval. $n = 5$ animals, 38 stimulating contacts, and 319 sessions.

(H) Literature comparison of ICMS behavioral detection (red) and neuronal activation (blue) threshold in rodents, non-human primates, and humans. Minimum reported or deduced values are plotted. a, Neuronexus³⁰; b, Neuronexus⁴⁴; c, Utah array¹⁵; d, Utah array¹⁷; e, Utah array¹⁴; f, Utah array⁴⁸; g, U-Probe⁴⁹; h, Pt/Ir microelectrode⁵⁰; i, Utah array⁵¹; j, IrO_x microelectrode¹⁶; k, Utah array.⁵²

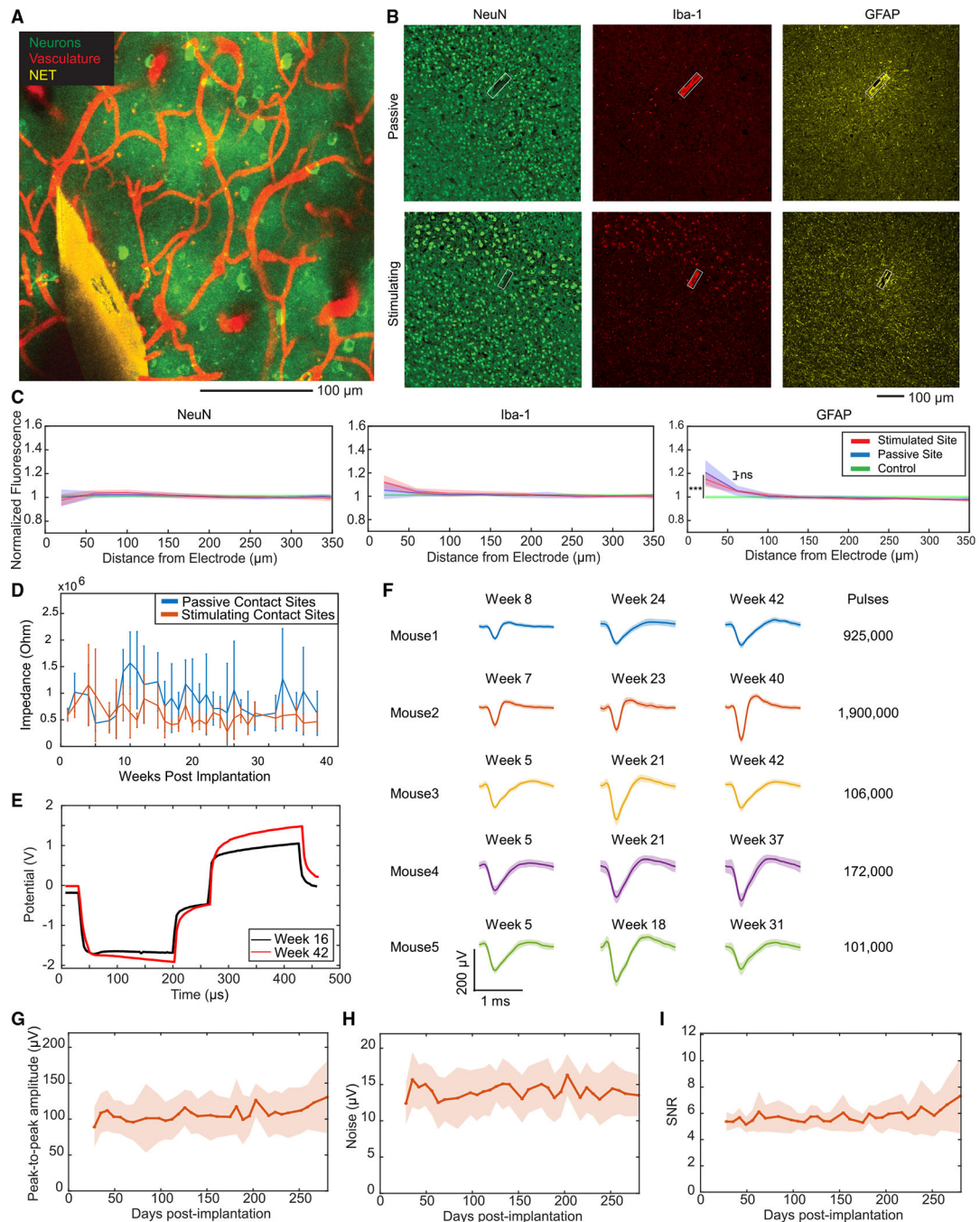


Figure 5. StimNETs maintain tight tissue-electrode integration and normal function after chronic ICMS

(A) Representative *in vivo* 2P MIP in a Gcamp6s mouse showing active neurons (green) and dense vasculature (red) around the StimNET.

(B) Representative immunostaining for NeuN, Iba-1, and GFAP showing normal neuronal density and little glial scarring or aggregation around StimNETs at both the passive and the stimulation sites. Green, NeuN; red, Iba-1; yellow, GFAP. Box encloses StimNET.

(C) Fluorescence intensity as a function of distance from StimNET of NeuN, Iba-1, and GFAP shows minimal disruption to local neuronal and glial cells from StimNET,

no significant difference between stimulating and passive contact sites, and significant difference between implanted and control tissue for only GFAP in the initial 40 μm from the implant surface (Kruskal-Wallis test with Dunn's *post hoc* correction). Fluorescence intensity was normalized to that from regions $>300 \mu\text{m}$ from the StimNET ($n = 5$ animals and 30 tissue samples). Shaded regions denote 95% confidence intervals. Controls: the contralateral cortical region in the same brain.

(D) Chronic impedance at 1 kHz showed no significant changes over time for stimulating contacts ($n = 5$ animals). Error bars denote 95th percentile confidence interval.

(E) Voltage transients at week 16 (day 114) and week 42 (day 293) post-implantation showing stability in charge injection after outputting 925,000 pulses *in vivo*.

(F) High SNR spike waveforms recorded by stimulation contacts, with time post-implantation and total stimulation pulse number indicated. Shaded area represents standard deviation. The number of spikes analyzed for each spike waveform at the three timepoints are mouse 1, $n = 311, 191, 81$; mouse 2, $n = 375, 125, 256$; mouse 3, $n = 64, 214, 470$; mouse 4, $n = 115, 225, 666$; and mouse 5, $n = 109, 196, 98$, respectively.

(G–I) Mean peak-to-peak amplitude (G), noise (H), and SNR (I) of recorded waveforms on stimulation contacts of a representative animal (mouse 2) over time. Each point is a metric averaged across all channels and sessions in a week. Shaded area represents standard deviation. Statistical significance: *** $p < 0.001$.

KEY RESOURCES TABLE

REAGENT or RESOURCE	SOURCE	IDENTIFIER
Antibodies		
Mouse anti-NeuN (1:100 dilution)	Millipore	Cat# MAB377X; RRID:AB_2149209
Chicken anti-GFAP (1:5000 dilution)	Abcam	Cat# ab134436; RRID:AB_2818977
Rabbit anti-Iba1 (1:1550 dilution)	Fujifilm	Cat# 015-28011
Goat Anti-Chicken Alexa Fluor® 647(1:200 dilution)	Abcam	Cat# ab150171; RRID:AB_2921318
Vectashield plus antifade mounting medium doped with DAPI	Vector Laboratories	Cat# H-2000-10
Experimental models: Organisms/strains		
Mouse: C57BL/6J-Tg(Thy1-GCaMP6s) GP4.3Dkim/J	The Jackson Laboratory	JAX: 024275
Mouse: C57BL/6J	The Jackson Laboratory	JAX: 000664
Software and algorithms		
MATLAB	MathWorks	R2021b
Custom MATLAB scripts for behavioral data analysis, neural recording analysis, 2P image processing, and the quantification of histological images.	This work	https://doi.org/10.5281/zenodo.7879485 ; https://github.com/XieLuanLab/StimNET
Psignfit toolbox	Heiko Schütt, AG NIP, University of Tübingen www.wichmann-lab.org with help from Stefan Harmeling, Jakob Macke and Felix Wichmann	v3.0
Violinplot-Matlab	Hoffmann H, 2015; violin.m - Simple violin plot using MATLAB default kernel density estimation. INRES (University of Bonn)	v1.7.0
ImageJ	Schneider et al., 2012 ⁶²	v1.53q
MJI	Sage et al., 2012 ⁶³	V1.5.0
COMSOL Multiphysics	COMSOL, Inc.	v5.6
Gamry Instruments Framework	Gamry Instruments, Inc.	V7.9.0
IBLrig software	International Brain Laboratory et al., 2021 ⁶⁴	v6.5.3
PrarieView Software	Bruker Inc.	v5.6
NIS-Elements software	Nikon Instruments Inc.	v5.21.00
ImageJ plugin 3D iterative segmentation (version 4.0.93)	Ollion et al., 2013 ⁶⁵	v4.0.93